Vertical Motions in Orographic Cloud Systems over the Payette River Basin. Part III: An Evaluation of the Impact of Transient Vertical Motions on Targeting during Orographic Cloud Seeding Operations

Kaylee Heimes, ^a Troy J. Zaremba, ^a Robert M. Rauber, ^a Sarah A. Tessendorf, ^c Lulin Xue, ^c Kyoko Ikeda, ^c Bart Geerts, ^b Jeffrey French, ^b Katja Friedrich, ^d Roy M. Rasmussen, ^c Melvin L. Kunkel, ^e and Derek R. Blestrud^e

^a Department of Atmospheric Sciences, University of Illinois at Urbana–Champaign, Urbana, Illinois
 ^b Department of Atmospheric Sciences, University of Wyoming, Laramie, Wyoming
 ^c Research Applications Laboratory, National Center for Atmospheric Research, Boulder, Colorado
 ^d Department of Atmospheric and Oceanic Sciences, University of Colorado Boulder, Boulder, Colorado
 ^e Department of Resource Planning and Operations, Idaho Power Company, Boise, Idaho

(Manuscript received 10 November 2021, in final form 15 August 2022)

ABSTRACT: In Part II, two classes of vertical motions, fixed (associated with vertically propagating gravity waves tied to flow over topography) and transient (associated primarily with vertical wind shear and conditional instability within passing weather systems), were diagnosed over the Payette River basin of Idaho during the Seeded and Natural Orographic Wintertime Clouds: The Idaho Experiment (SNOWIE). This paper compares vertical motions retrieved from airborne Doppler radial velocity measurements with those from a 900-m-resolution model simulation to determine the impact of transient vertical motions on trajectories of ice particles initiated by airborne cloud seeding. An orographic forcing index, developed to compare vertical motion fields retrieved from the radar with the model, showed that fixed vertical motions were well resolved by the model while transient vertical motions were not. Particle trajectories were calculated for 75 cross-sectional pairs, each differing only by the observed and modeled vertical motion field. Wind fields and particle terminal velocities were otherwise identical in both trajectories so that the impact of transient vertical circulations on particle trajectories could be isolated. In 66.7% of flight-leg pairs, the distance traveled by particles in the model and observations differed by less than 5 km with transient features having minimal impact. In 9.3% of the pairs, model and observation trajectories landed within the ideal target seeding elevation range (>2000 m), whereas, in 77.3% of the pairs, both trajectories landed below the ideal target elevation. Particles in the observations and model descended into valleys on the mountains' lee sides in 94.2% of cases in which particles traveled less than 37 km.

KEYWORDS: Orographic effects; Updrafts/downdrafts; Vertical motion; Cloud seeding

1. Introduction

Precipitation enhancement from seeding wintertime orographic cloud systems has been attempted in research and operational projects for nearly seven decades (Rauber et al. 2019). The sophistication of research during this period has advanced from studies in the 1960s that relied on snow gauges and rawinsondes (e.g., Mielke et al. 1970) to recent experiments utilizing numerical models, polarization and airborne radars, and cloud physics instrumentation (Tessendorf et al. 2019). One limitation in evaluating the impacts of seeding orographic clouds has been our poor understanding of vertical air circulations in orographic environments and the ability of models to accurately simulate these circulations.

Comparisons of observed orographic updraft structures with model-resolved updraft structures were first reported by Garvert et al. (2007). They compared airborne dual-Doppler derived flow over the Cascade Mountains with MM5. Vertical air motions w were obtained using a downward integration of the anelastic continuity equation with w = 0 at the top of their cross sections at 5 km above mean sea level (MSL). They found that two distinct scales of mesoscale-wave-like air

 ${\it Corresponding\ author}. \ Kaylee\ Heimes, kheimes 2@illinois.edu$

motions were present: a vertically propagating mountain wave anchored to the Cascade crest and ~20-km-wavelength undulations triggered by interaction of along-barrier flow with ridge and valley topographic features normal to the Cascade crest. A limitation was that derived vertical motion fields associated with topographically generated gravity waves were forced by the upper boundary condition to stop at the top of the cross section while model gravity waves extended above 5 km. More recently, Chu et al. (2017a,b) used the WRF large-eddy simulation (LES) 100-m-resolution model and observations from the Wyoming Cloud Radar (WCR) to compare updraft structures in a shallow, largely blocked stratiform cloud and orographic convection with model-derived updrafts. The model was shown to capture the updraft structures well at fine resolution and in the stratiform and convective.

Geerts et al. (2011) was the first attempt to investigate how observed updraft structures affect the path natural hydrometeors take as they move across a mountain range. They derived particle streamlines within orographic flow over the Medicine Bow Mountains of Wyoming using airborne vertical-plane dual-Doppler (VPDD) analysis, which combined the along track component of the wind and the vertical particle velocity. Their method does not require assumptions about particle fall

speed or airmass continuity integration constraints. Their calculations showed that the vertical wind profile influenced the slope of the particle streamlines near the mountain and determined which streamlines hit the mountain. Geerts et al. (2015) subsequently used VPDD to create streamlines of the true vertical and horizontal motion of hydrometeors. VPDD streamlines were used below the flight path in four storms with different updraft structures over the same region. They found that updraft structures and horizontal wind speed influenced the slope of the particle streamlines, which changed where the precipitation fell.

Model large-eddy simulations of orographic updraft structures have employed a wintertime silver iodide (AgI) seeding parameterization (WASP) in studies of seeding impacts (Xue et al. 2013a,b, 2014, 2016, 2017; Chu et al. 2014). These studies found that the 100-m LES simulations captured small-scale features that influence particle dispersion in the boundary layer where shear turbulence and vertically oriented buoyancy eddies were responsible for the vertical transport of AgI. For ground-based seeding, the particles were confined within the boundary layer where most particles rose above 600 m and a few particles reached 3600 m (Xue et al. 2016).

Although large-eddy simulations provide insight about the influence of fine-scale features on particle trajectories, the computation requirements of these simulations make it impractical for use in operational seeding. For example, Idaho Power Company (IPC) currently uses a 1.8-km-resolution model to plan and evaluate their wintertime operational seeding program in Idaho. A key component of the Seeded and Natural Orographic Wintertime Clouds: The Idaho Experiment (SNOWIE) was to evaluate the use of the 900-m model as a tool for targeting precipitation enhancement in the Payette River basin.

Since the first orographic cloud seeding experiments, a common motivation has been to understand the trajectories of ice particles generated by seeding. Particle trajectories were first reported by Hobbs (1975a,b), who employed a simple trajectory model based on rawinsonde winds and assumed particle terminal velocities. A similar, simple trajectory model was applied during seeding experiments over the Sierra Nevada Range (Rauber et al. 1988). These studies and others (e.g., Holroyd et al. 1988) assumed simple laminar flow over the mountain range when calculating trajectories.

As part of SNOWIE, Zaremba et al. (2022a) developed a method to retrieve local vertical air velocity w and flight-legaveraged particle terminal velocity profiles \overline{V}_t from airborne radial velocity measurements. Using this retrieval method, Zaremba et al. (2022b) categorized updrafts in wintertime cloud systems over the Idaho mountains as fixed, that is, mechanically driven by the terrain and locked to the terrain under a given ambient wind and stability profile (i.e., vertically propagating gravity waves), and transient, temporally varying vertical circulations related to vertical wind shear, conditional instability, and thermodynamic effects such as evaporation within passing weather systems. The common presence of these transient vertical circulations during SNOWIE raised the question as to their impact on cloud seeding.

This paper examines the impact of fixed versus transient updrafts in orographic environments on the trajectories of ice particles created by airborne seeding. To address this question, we first compare updraft structures retrieved from analysis of high-resolution airborne radar data collected during SNOWIE with updrafts simulated by a 900-m-horizontalresolution simulation of these storms using the WRF Model. We show that the WRF simulation captures the fixed circulations forced by the orography but not the subgrid-scale transient circulations associated with instability and shear. Twodimensional trajectories of particles are then calculated using identical horizontal wind and terminal velocity fields, but different updraft structures based on the observations and model simulation. The trajectory analysis is two-dimensional to conform to the available radar retrievals of vertical air motion from the University of Wyoming King Air (UWKA) WCR (Zaremba et al. 2022a,b) and the findings (the impact of the scale of vertical motions on the final fate of a seeded trajectory) is limited to two dimensions. The impact of the fine-scale updraft structures on targeting during seeding are then assessed to determine whether a 900-m-resolution simulation is sufficient for accurate targeting of seeding operations within the Payette River basin.

2. Orography of the Payette River basin

The Salmon River Mountains are a block-shaped massif in the central part of the state of Idaho (Fig. 1). The Payette River and its tributaries drain the south and west side of the mountain massif. The Payette River basin consists of a series of ridges and valleys that run primarily north-south. The ridges reach elevations of ~2.5-2.8 km while the upper valleys have elevations of ~1.4 km, descending to ~0.9 km along the South Fork of the Payette River. The target area for seeding by IPC is the mountainous region feeding water into the Payette River basin. Water from particles landing beyond that basin would not flow through their dam structures. At Payette, Idaho, the Payette River extends upstream eastward from the Snake River and later splits into the North Fork, Middle Fork, and South Fork. The IPC targets mountains above ~2000 m within the basin surrounding the South and Middle Forks. The target altitude constraint is to ensure that particles contribute to the snowpack, so that the precipitation contributes to a more continuous flow in the river system (and a continuous flow of electricity) rather than the pulse of streamflow that would be produced if the particles melted and fell as rain. Targeting elevations greater than 2000 m increases the snowpack at higher elevations, which lengthens the runoff season because the snowpack survives longer into the spring and summer. The North Fork has a narrow drainage area and is located near the Weiser basin, which floods often, making it less than ideal to target for cloud seeding.

The UWKA flew back and forth (typically west-east, or southwest-northeast) legs during SNOWIE along one of three tracks over the Payette River basin parallel to the midlevel (~700 hPa) flow. On the west-east flight track (A on Fig. 1) the UWKA crossed the southern end of the Western Range, the North Fork Range, and the Western and Eastern Salmon

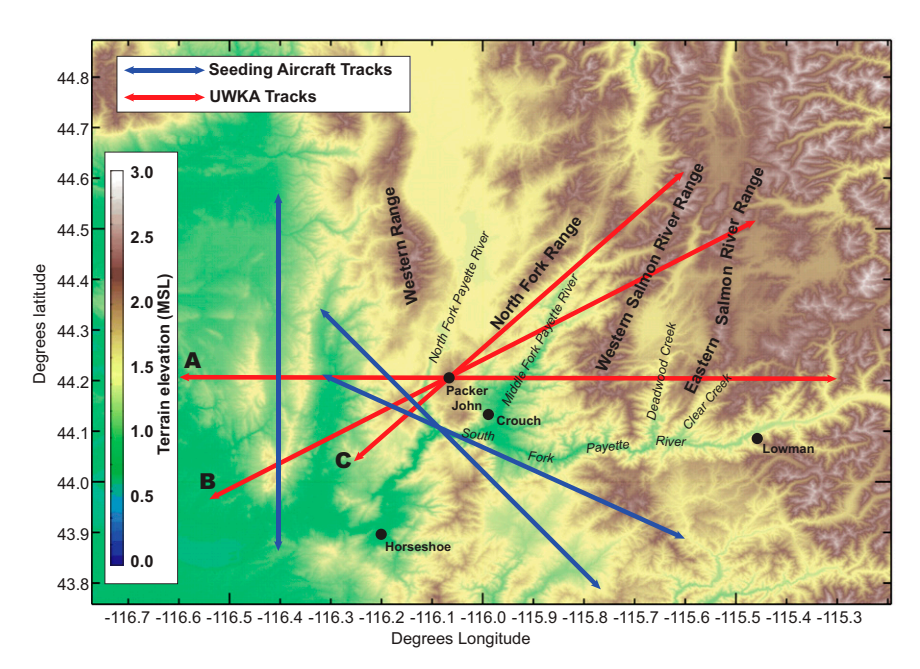


FIG. 1. Terrain map of the SNOWIE region. The red flight tracks were the three used by the UWKA. The blue tracks were used by the WMKA seeding aircraft.

River ranges, as well as the Payette River tributaries between these ranges. On track B, the UWKA flew over the same ranges but at an ~40° angle to the ridge lines. On track C, the UWKA crossed the Western Range and flew along the eastern side of the North Fork Range crossing the pass at the northern limit of the Middle Fork of the Payette River. A Weather Modification, Inc., King Air (WMKA) aircraft flew upwind of, and perpendicular to the UWKA flight tracks. Vertical motions observed during SNOWIE reported in this paper were associated with forcing fixed to the mountain ranges within the Payette River basin and transient circulations within passing weather systems (Zaremba et al. 2022b).

3. Data

a. WCR

The WCR, a pulsed Doppler radar with a frequency of 95 GHz, was flown on the UWKA aircraft (Research Flight Center 2017a,b). The WCR antennas were oriented nominally at zenith and nadir providing measurements of radial velocity V_r at a vertical resolution of ~30 m and a horizontal resolution of 4.5-7.5 m, depending on ground speed. The WCR recorded V_r between the ground and cloud top. The V_r measurements were not obtained in a 250-m zone surrounding the UWKA. Vertical air motions and vertical profiles of reflectivityweighted mean terminal velocity \overline{V}_r were retrieved from V_r measurements using aircraft pitch, roll, yaw, and airspeed measurements, together with winds from rawinsondes using the algorithm described in Zaremba et al. (2022a). The w data were then regridded using the nearest neighbor method to a 4.5-7.5-m horizontal \times 30-m vertical grid referenced to MSL. The UWKA flew in the along-wind direction for 23 intensive

operation periods (IOPs) with a total of 238 flight legs during SNOWIE. The WMKA intersected the UWKA flight tracks during 19 IOPs (Fig. 1).

The WCR also measured the equivalent reflectivity factor Z_e . The WCR reflectivity is calibrated by measuring the return from a trihedral corner reflector with a known scattering cross section. Error associated with this calibration is estimated to be less than 2.5 dB at and away from the radar flight level (Wendisch and Brenquier 2013, chapter 9.5.5, 509–517; Grasmick et al. 2022). The minimum detectable signal was \sim 40 dB Z_e at 1-km distance away from the radar and \sim 26 dB Z_e at a distance of 5 km.

b. WRF Model

During the winter season of 2016/17, WRF, version 3.9.1.1, was run in a continuous simulation starting on 1 October and ending on 30 April, which included the entire SNOWIE campaign between 7 January and 16 March 2017 (Tessendorf et al. 2019). Hourly WRF output of vertical circulations over the Payette River basin and adjacent mountains from the SNOWIE period are compared herein with retrieved vertical circulations derived from measurements of V_r from the WCR obtained during SNOWIE. Initial and boundary conditions were input from the 31-km-resolution European Centre for Medium-Range Weather Forecasts ERA-Interim data. The outer WRF domain had a 2.7-km horizontal resolution and a nested inner 900-m-resolution domain centered over central Idaho. In the vertical direction, WRF had 81 terrain following levels between the surface and 20 hPa distributed with 23 levels below 1000 m above ground level (AGL) and 43 levels below 3000 m AGL. The Thompson and Eidhammer aerosol-aware microphysics scheme (Thompson and Eidhammer 2014), the Mellor-Yamada-Nakanishi-Niino level-2.5 planetary boundary layer scheme (Nakanishi and Niino 2006), the Noah-MP land surface model (Niu et al. 2011), and the Rapid Radiative Transfer Model (RRTMG; Iacono et al. 2008) were employed.

c. Rawinsondes

Data from rawinsondes launched at the nearest hour to the flight leg were used herein to assess the background shear and stability for each case presented. Equivalent potential temperature θ_e with respect to water was calculated using Bolton (1980) to determine regions of potential instability. The bulk Richardson number R_b was calculated from rawinsonde data that were averaged over 20 data points ($\sim 100 \, \mathrm{m}$) using a centered rolling mean and resampled using linear interpolation every 100 m. The R_b was calculated using the formula

$$R_b = \frac{g}{\theta_v} \frac{\frac{\Delta \theta_v}{\Delta z}}{\left(\frac{\Delta u}{\Delta z}\right)^2 + \left(\frac{\Delta u}{\Delta z}\right)^2},$$

where g is gravity, $\overline{\theta}_v$ is the mean virtual potential temperature, θ_v is the virtual potential temperature, u is the west–east wind component, v is the north–south wind component, and z is height.

Lockheed Martin LMS6 rawinsondes used in this paper were launched by IPC at Crouch and Lowman, Idaho (Blestrud 2018, 2021). The manufacturer-stated accuracy of wind speed measurements was ± 0.2 m s⁻¹, $\pm 5\%$ for relative humidity, and ± 0.2 °C for temperature. The rawinsonde data typically had an average temporal resolution of 1 s, vertical resolution of 4 m, and the sondes drifted ~12.4 km from their launch location before reaching cloud top.

4. Model comparison with retrieved updrafts

The findings in Zaremba et al. (2022b) motivated the comparison of vertical cross sections of w in the 900-m WRF simulation (w_F) to the retrieved w from the WCR (w_R). Zaremba et al. (2022b) describes the environments that led to transient updraft and downdrafts embedded within fixed, orographically forced vertical circulations. The transient features embedded within fixed, orographically forced updrafts were common during cloud seeding missions and may have had an impact on targeting.

a. Quantitative methodology to evaluate fixed versus transient circulations

An orographic forcing index (OFI) was developed to quantitatively assess the degree to which vertical circulations observed or modeled along individual cross sections were associated with fixed, orographic vertical circulations versus transient circulations associated with passing weather systems following Zaremba et al. (2022b). To develop the index, it was assumed that fixed, orographic updrafts associated with orographically induced vertically propagating gravity waves occur over positively sloped terrain (upslope, where the terrain height increases eastward between two points) and downdrafts over negatively sloped terrain (downslope, where the terrain height decreases eastward between two points), while

transient updrafts occur randomly and vary in time, largely without regard to the underlying terrain features.

Let m be the number of grid elevations between 4 km and the terrain and n be of the number of grid columns along a given cross section. Only grid points below 4 km were considered because the seeding height was at \sim 4 km in most cases so only the vertical circulations below 4 km influence particle trajectories. Let the total number of grid points on the cross section between the 4-km level and the terrain be N (approximately $m \times n$, with adjustment for variation in terrain height). For each grid point (m_i, n_j) between 4 km and the terrain, if the slope at the base of $n_j > 0$ and $w(m_i, n_j) > 0$ or the slope at the base of $n_j < 0$ and $w(m_i, n_j) < 0$ an index $I(m_i, n_j)$ was set to 1. Otherwise $I(m_i, n_j)$ was set to 0. Then OFI is given by

$$OFI = \frac{\sum_{m} \sum_{n} I_{m,n}}{N} \times 100\%.$$

In simple terms, the OFI is a count of the number of grid points for which updrafts reside over upslope terrain and downdrafts reside over downslope terrain. A higher OFI corresponds to a higher prevalence of orographically forced updrafts and a lower OFI corresponds to more transient updrafts. For purely orographically forced updrafts the value of OFI should approach 100% since updrafts will be present over upward-sloping terrain and downdrafts over downwardsloping terrain. For transient circulations within passing weather systems, the value of OFI should approach 50% since there is a near equal probability that an updraft or a downdraft might be present over terrain with either slope, with the exception that surface-based convection may be triggered more often on the upwind side of a range. Figures 2a and 2b show WCRretrieved updrafts (red) and downdrafts (blue) and WRFsimulated updrafts and downdrafts (same colors) for an example cross section, while Figs. 2c and 2d show $I(m_i, n_i)$ classifications for these circulations. In Fig. 2 the terrain slope is green where positive and blue where negative. In Figs. 2c and 2d, $I(m_i, n_i) = 1$ where gray and $I(m_i, n_i) = 0$ where red. The value of OFI for Fig. 2c (WCR) was 56.2% and Fig. 2d (WRF) was 60.9%.

OFI was calculated for the observations (OFI $_R$) and the model (OFI $_F$) for each of the 75 flight legs where trajectories could be calculated. The distributions of OFI $_R$ and OFI $_F$ (Fig. 3) are distinct. The mean value of OFI $_R$ was 51.8% indicating that transient circulations were common below 4 km during the flights. The mean value of OFI $_F$ was 61.6%, with 52 out of 75 cross sections exhibiting OFI $_F$ values exceeding 60%, with 4 cross sections exceeding 80%. This analysis shows that in most cases the model simulated the orographically forced updrafts but did not have the resolution to capture smaller-scale transient features.

b. Comparison of WCR and WRF vertical circulations during SNOWIE

The 900-m simulation is not expected to resolve transient updrafts and downdrafts with scales of less than a few kilometers. As shown in Zaremba et al. (2022b), vertical transient circulations over the Payette River basin often occur on smaller scales. We present below four examples comparing

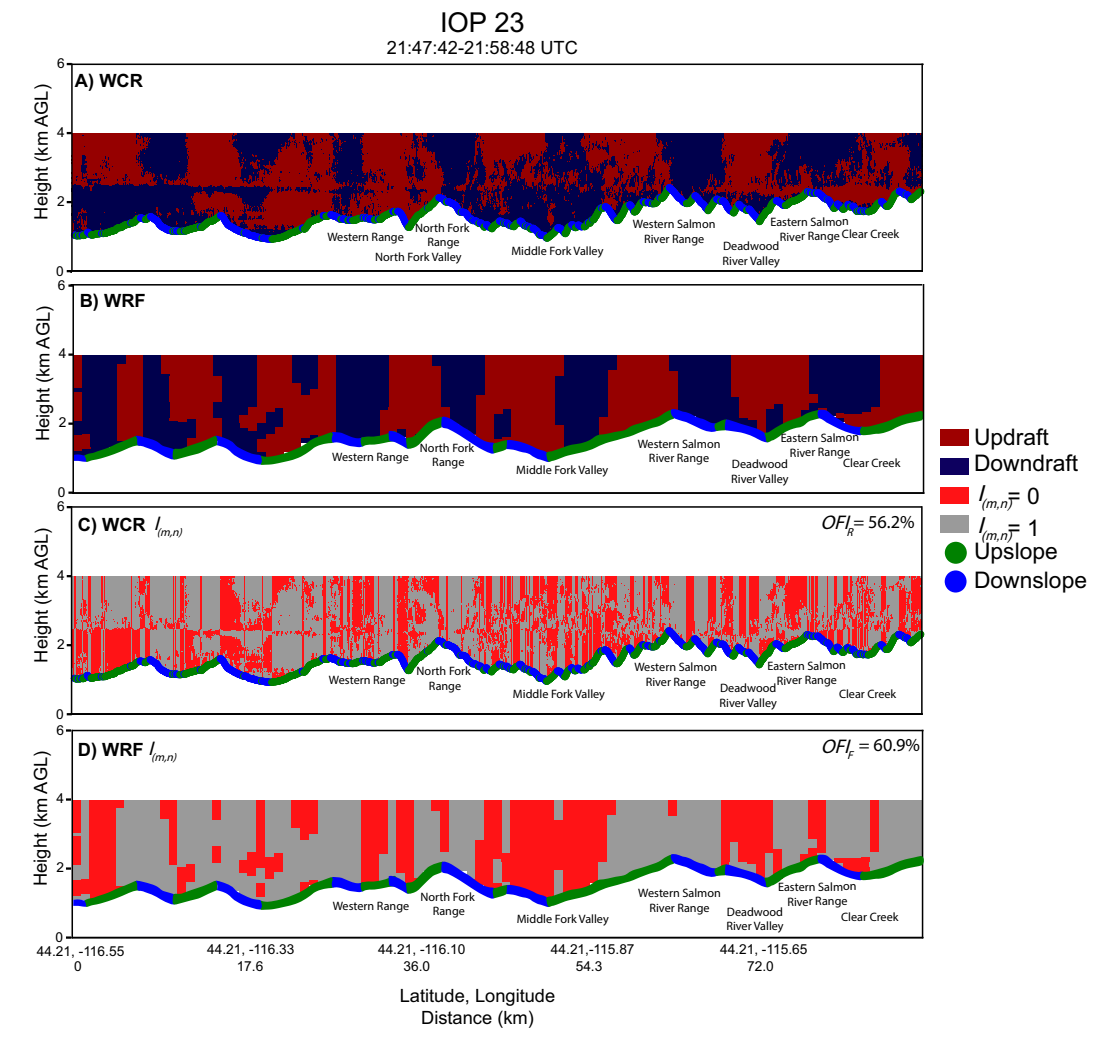


FIG. 2. Vertical cross sections for IOP 23 2147:42–2158:48 UTC 9 Mar 2017: (a) w_R , where updrafts are red and downdrafts are dark blue, (b) w_F , where updrafts are red and downdrafts are dark blue, (c) grid points where $I_{(m,n)} = 1$ are shaded gray and points where $I_{(m,n)} = 0$ are shaded red for the WCR cross section in (a), and (d) grid points where $I_{(m,n)} = 1$ are shaded gray and points where $I_{(m,n)} = 0$ are shaded red for the WRF cross section in (b). In all panels, positively sloped (upslope) terrain is green and negatively sloped (downslope) terrain is blue.

the WCR-retrieved and WRF-calculated updrafts. In the first, the 900-m model accurately simulated fixed updraft structures in the absence of transient updraft features. In the second, the model simulated orographically forced features but not the transient features. In the third, the model deviated from the observations because only transient features were present. In the fourth, transient features were present primarily above the seeding level. These four comparisons represent the range of scenarios concerning model agreement with observed circulations. We conclude this section with a summary of OFI for the 75 flight legs where both WCR and WRF cross sections were available.

1) FIXED OROGRAPHIC UPDRAFTS (IOP 23, 9 MARCH 2017)

IOP 23, flight leg (FL) 2147:42–2158:48 UTC is an example in which w_F closely resembled w_R . During this flight leg, a

deep, stratiform orographic cloud was present with 9-km echo tops (all heights MSL) and relatively uniform radar reflectivity at all altitudes (Fig. 4a). A melting layer was present at ~2.3 km, sloping downward slightly to the east. Winds were variable and less than 2 m s⁻¹ below 1.85 km, increasing to $6 \text{ m s}^{-1} \text{ from } 220^{\circ} \text{ at } 2.3 \text{ km}, 13 \text{ m s}^{-1} \text{ from } 250^{\circ} \text{ at } 2.5 \text{ km},$ and 20 m s⁻¹ from 270° at 4 km. The cloud was stable based on the profile of θ_e , and shear-induced turbulent circulations were not present based on the profile of R_b . Deep orographically forced waves were present with weak mechanically induced boundary layer turbulence. Since OFI was calculated below 4 km, the boundary layer turbulence reduced the OFI_R to 56.2% despite the deep, orographic updrafts. The orographically forced waves start at the crest of the mountain and extend to cloud top with rising air on the upwind side of the mountain and descending air on the downwind side, with

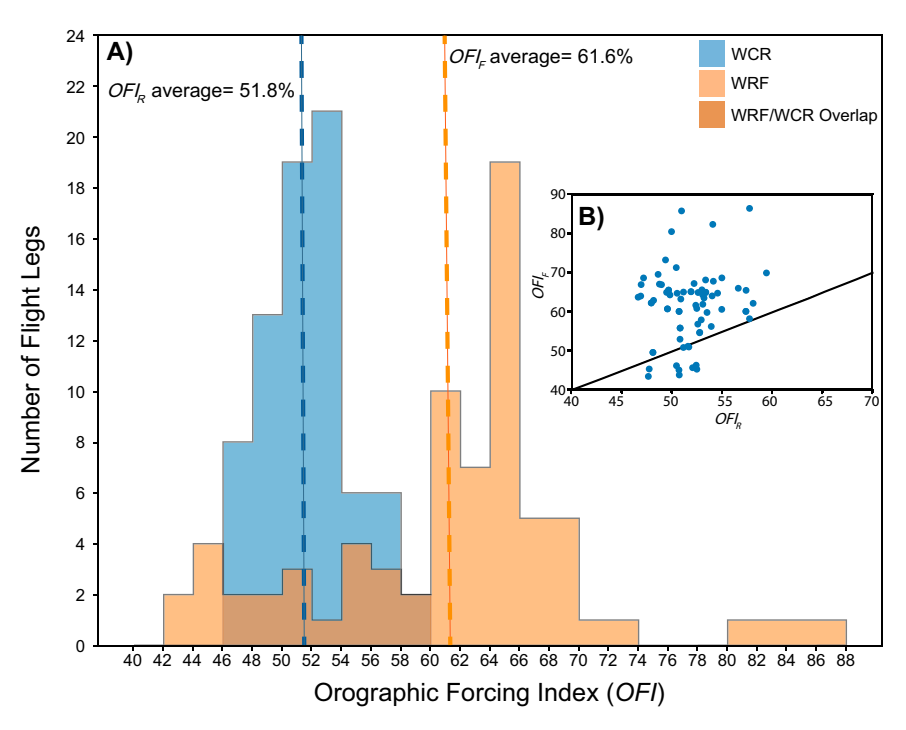


FIG. 3. (a) A histogram of the OFI_R and OFI_F for the 75 cross sections where particle trajectories could be calculated. The dashed line indicates the average OFI_R and OFI_F . Light-blue colors represent OFI_R , and light-orange colors represent OFI_F . (b) An inset with a scatterplot of OFI_R versus OFI_F , where each pair of particle trajectories is represented by a blue dot. The black line is the one-to-one line.

a single standing wave over the Middle Fork valley. These waves, generated above each mountain slope, had updraft magnitudes of \sim 0.3–0.5 m s⁻¹. A cross section through the 900-m WRF simulation for the same coordinates as Figs. 4a and 4b shows almost identical updraft structures as the observations (Fig. 4c). OFI_F was 60.9%, which was less than 5% greater than OFI_R. In both Figs. 4b and 4c, rising air is generated along every upwind mountain slope and descending air along the leeward slope, with vertical circulations extending from the crest of the mountain to the height of the observed cloud top. The model also simulated the standing wave over the Middle Fork valley. The magnitude of the modeled orographically forced waves was $\sim 0.3-0.5$ m s⁻¹ matching the observations. The horizontal wavelength of the orographically forced waves was approximately 15 km, significantly greater than the 900-m horizontal resolution of the model, making it possible for the orographically forced waves to be well resolved in the 900-m simulation.

2) FIXED AND TRANSIENT UPDRAFTS (IOP 17, 21 FEBRUARY 2017)

Figure 5 shows a cross section from IOP 17 at 1534:12–1553:27 UTC. A 6-km-deep cloud was characterized by orographically forced waves along with shallow surface-based convection, that is, air rising from the surface as a result of potential instability. Rawinsondes launched at the nearest hour to the flight leg show wind speeds at \sim 2.5 m s⁻¹ from the south at the surface increasing to \sim 10 m s⁻¹ from the south at

1.4 km. Between 1.5 and 2.2 km the winds veer with height to 220° and increase to \sim 20 m s⁻¹. From 2.2 to 5.8 km the wind speed was out of the southwest and never exceeded 30 m s⁻¹. The θ_e decreased with height from the surface within the valley to ~3 km, indicating a potentially unstable atmosphere favorable for convection originating along the terrain. The weak wind shear in the presence of potential instability led to $R_b > 0.25$ above 1.5 km so that shear-induced turbulence was unlikely (Fig. 5a). Figure 5b shows shallow surface-based convection extending from the mountain crest to 3 km with deeper convection on the windward side of the mountains extending to the cloud top at 6 km. OFI_R for this case was 51%. The updrafts associated with the convection reached 3-4 m s⁻¹ with the stronger updrafts associated with the enhanced lift from the mountains. Figure 5c from the model captures the orographically forced updrafts but does not simulate the smaller-scale convective features. The magnitude of the simulated updrafts reached ~ 3 m s⁻¹, which is weaker than the observed updrafts. In this case, the stronger updrafts in the observations associated with smaller-scale convection were not resolved by the model. An OFI_F of 85.8% further supports the model's ability to resolve the orographic structures but not the transient structures.

3) Transient updrafts (IOP 15, 19 February 2017)

During some IOPs the dominant updraft structures were transient. Figure 6 from IOP 15 1921:32–1939:07 UTC shows w_R in an environment in which θ_e decreases with height from

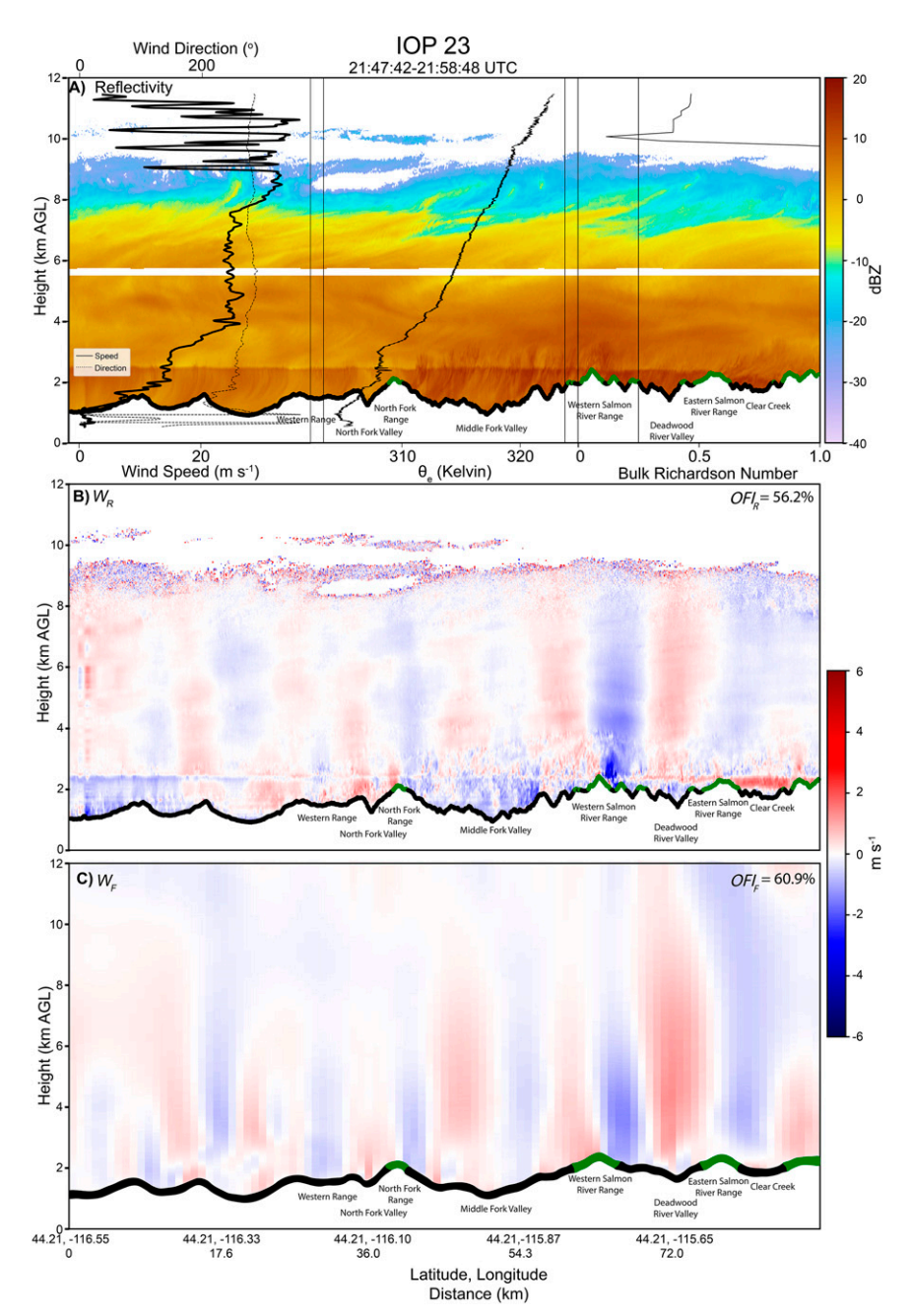


FIG. 4. Vertical cross sections from IOP 23 2147:42–2158:48 UTC 9 Mar 2017: (a) Z_e , with wind speed (thick line), wind direction (thin line), θ_e , and R_b from the rawinsonde launched at 2200 UTC from Lowman overlayed (the data extend below the topography because the soundings were launched from a river valley), (b) w_R retrieved from WCR data, and (c) Simulated w_F from WRF. In all panels, terrain <2000 m and below the IPC target elevation is colored black. Terrain with elevations >2000 m and within the IPC target elevation is colored green.

the valley to \sim 7 km indicating the presence of potential instability supportive of deep surface-based convection. The winds were less than 5 m s⁻¹ below 2.4 km and above 2.4 km increased to 21 m s⁻¹ by 8 km at a nearly continuous rate. Above 2.4 km the wind direction was between 230° and 240°. This case is further discussed in Zaremba et al. (2022b). Figure 6b from the observations shows that there was only

weak orographic forcing while the main source of updrafts was the convection near the center of the cross section. This was reflected in an OFI_R value of 50.8%. The convective updraft had maximum values of ~ 4 m s⁻¹ while the rest of the cloud contained updrafts of ~ 1 m s⁻¹. The cross section from the model in Fig. 6c shows that the convection was not resolved, while the updrafts and downdrafts within the model

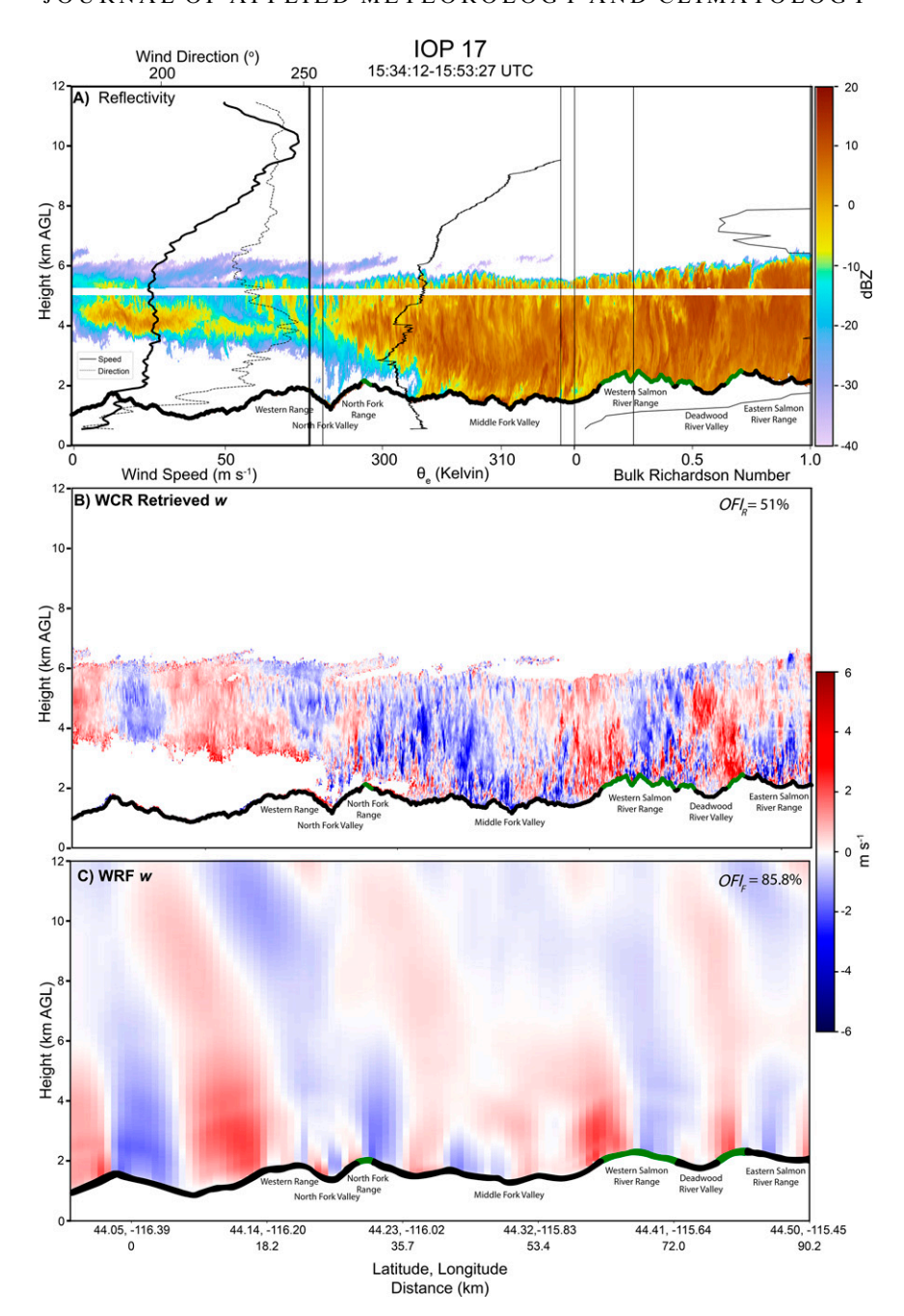


FIG. 5. As in Fig. 4, but for IOP 17 at 1534:12–1553:27 UTC 21 Feb 2017. Overlayed rawinsonde data were from the rawinsonde launched at 1600 UTC from Crouch.

were not always in phase with the mountain slopes. As a result, the OFI_F was 54.3%, near the mean value expected for transient circulations.

4) Transient updrafts above seeding level (IOP 16, 20 February 2017)

Figure 7b shows a cross section from 1538:42 to 1558:40 UTC 20 February 2017 in which observed vertical circulations were associated with shear turbulence. Zaremba et al. (2022b) discuss

this case in more detail. Rawinsonde data in Fig. 7a show variable horizontal winds in the valley that did not exceed 5 m s⁻¹ below 1.7 km. Above 1.7 km, wind speeds increase from 5 to 25 m s⁻¹ at 4.6 km while winds veered from 163° to 237°. From ~5.6 to 8 km wind speeds increased from 28 to 57 m s⁻¹ and were nearly constant at ~255°. Within this region, θ_e increased with height, indicating a stable atmosphere. Strong shear and a stable atmosphere between 5.6 and 8 km caused R_b to approach 0.25 in the layer supporting shear-generated turbulence.

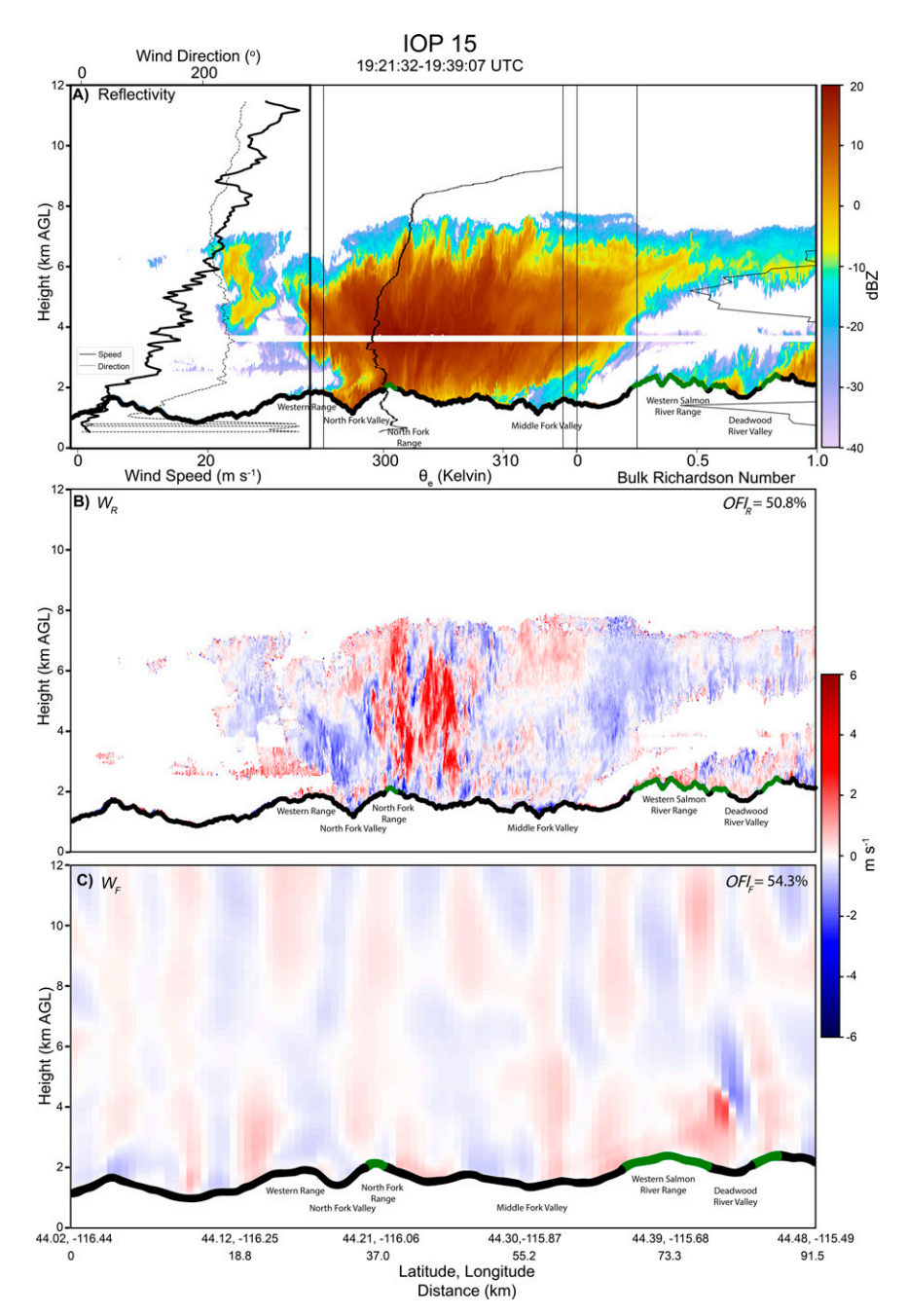


FIG. 6. As in Fig. 4, but for IOP 15 at 1921:32–1939:07 UTC 19 Feb 2017. Overlayed rawinsonde data were from the rawinsonde launched at 1900 UTC from Crouch.

The shear-generated vertical circulations were associated with w values ranging up to ± 10 m s⁻¹. Weaker turbulence below 5 km was also present associated with wind shear near the terrain. There was weak ascent due to orographically forced updrafts, however, these updrafts have vertical circulations of ~ 1 m s⁻¹, significantly weaker than the vertical circulations generated by shear turbulence. Despite the strongest transient features occurring above the altitudes used to calculate OFI, OFI $_R$ was 49.7%. As shown in Fig. 7c, the updraft

structures associated with shear turbulence were on scales smaller than 900 m and were not resolved by the model. For this reason, the w_F cross section does not show turbulent, small-scale vertical circulations and instead shows orographically forced updrafts, and underestimates the maximum updraft speeds by \sim 7 m s⁻¹. The model captures the rising motion on the upwind side of the mountains similar to the observed updrafts, but the model smears the orographically forced updrafts in the horizontal across the high shear layer

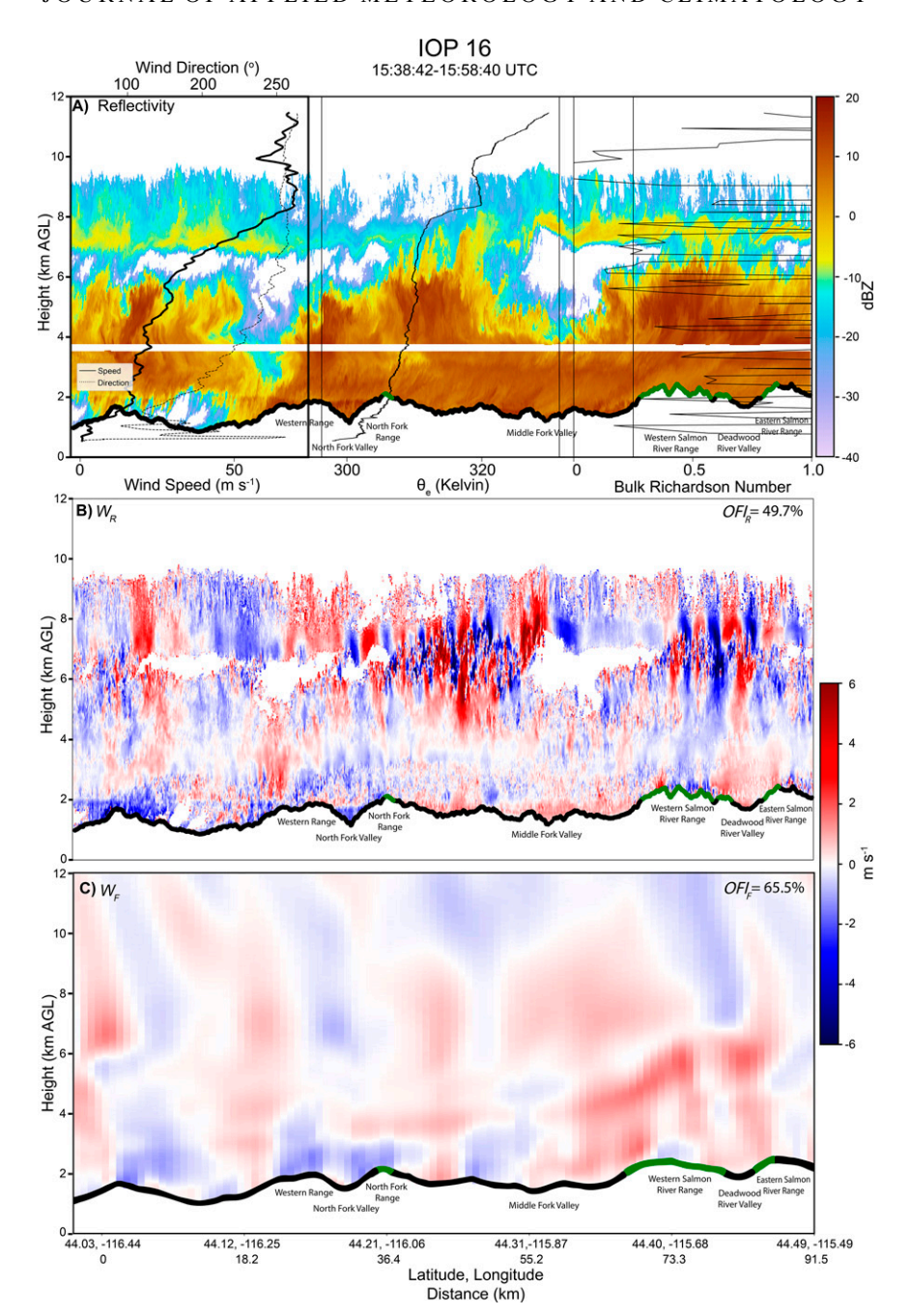


FIG. 7. As in Fig. 4, but for IOP 16 1538:42–1558:40 UTC 20 Feb 2017. Overlayed rawinsonde data were from the rawinsonde launched at 1500 UTC from Crouch.

above 4 km. Below 5 km along the windward side of the Western and Eastern Salmon River Range, the model produced updrafts over the windward slopes. These differences are reflected in a OFI_F that was 65.5%, ~15% greater than OFI_R .

5. Calculation of particle trajectories

The purpose of this study is to quantify the impact of transient updrafts and downdrafts on trajectories of snow particles

created by airborne seeding over the Payette River basin during SNOWIE. Two particle trajectories were calculated for each cross section in each IOP where radar data from the WCR was available and seeding was conducted by the WMKA. Here, T_R was calculated using the retrieved w_R field within the cross section, and T_F was calculated using the modeled w_F field. In both calculations, identical horizontal wind fields from WRF at the closest hour to the flight leg were used and identical terminal velocity profiles retrieved using the

TARIE 1	Outcomes	for	103	nairs	α f	trai	ectories
I ADLE 1.	Outcomes	101	103	pans	OI	uap	cetories.

T_R and T_F both land in radar-observed domain	T_R and T_F exit east edge of the domain	T_F lands in domain; T_R exits east edge of domain	T_R lands in domain; T_F exits east edge of domain	No echo within 820 m below point <i>P</i>	Plane turned; w_R could not be retrieved	T_R exits the top of cloud
75	8	2	4	12	1	1

Zaremba et al. (2022a) algorithm. As an experiment, trajectories were also calculated using horizontal winds from rawinsondes launched at the nearest hour. The results were similar to those using the complete WRF horizontal wind fields. Here we use horizontal winds from WRF because they provide more realistic winds over the complex terrain. It was assumed that seeding occurred where supercooled liquid water was present, and particles initiated by seeding grew to the size of the particles in the sample volume. The only difference between the trajectories was due to differences between the w_R and w_F fields. Cross sections of w_F were made at the nearest hour to the UWKA flight leg and through the same latitude and longitude coordinates as the flight leg.

The WMKA burned AgI flares that initiated ice particle formation from the WMKA flight level down to 820 m below the aircraft, based on the burn time of the flares falling at their terminal velocity. The 820-m value was provided by Weather Modification Incorporated from their independent measurements. Since AgI flares initiated particle growth down to 820 m below flight level, there is a range of particle landing locations. For the purposes of this study, the latitude and longitude of the point P where the WMKA track intersected the UWKA track was recorded and used as the start location for both T_R and T_F . In cases in which no radar echo was present at P, the start height of T_R and T_F was lowered until the particle was within radar echo, provided that the radar echo was no more than 820 m below P. If the echo top was more than 820 m below P, T_R and T_F were not calculated.

Trajectory calculations were made every second where the particle's next position in the horizontal was determined by the along flight component of the horizontal wind derived from WRF at the closest hour and in the vertical direction by $w_R - \overline{V}_t$ for T_R and $w_F - \overline{V}_t$ for T_F . The particle trajectory was stopped when the particle intersected the terrain or when the particle exited the east side of the domain. Of the 103 trajectory pairs calculated, 9 encountered the melting level. The \overline{V}_{i} , retrieved from the Zaremba et al. (2022a) algorithm accounted for the change in terminal velocity from ice particles to water drops across the melting level. However, the retrieval of w_R within the melting level itself has a large uncertainty (Zaremba et al. 2022a). The impact of this uncertainty on the trajectories was minimal because the melting level was very close to the terrain (<500 m) in all but one trajectory, and particles passed through the melting level in under a minute.

For T_R , particle trajectories sometimes intersected regions where the w_R data were missing. This occurred when the particle crossed the 250-m zone surrounding the UWKA, where a hole in the radar echo was present, or if a beam of radar data was missing. Since \overline{V}_t from the observations were used

when calculating T_F , T_F trajectories also had missing \overline{V}_t information at altitudes corresponding to the 250-m zone surrounding the UWKA. To fill in the missing values of w_R and \overline{V}_{t} in the 250-m zone surrounding the UWKA, the values of w_R and \overline{V} , within this zone were linearly interpolated from the first valid points above and below the UWKA altitude. In cases in which T_R encountered a hole in cloud echo, it was assumed that no vertical motion was present within the hole and the particle trajectory through the hole was calculated setting $w_R = 0$. Most holes in the w_R data were less than 300 m wide, with the largest being 2964 m. Tests were performed first excluding all flight legs where holes >300 m wide were present and then including all flight legs regardless of the size of the holes. The results of these tests showed that excluding the legs with larger holes had almost no impact on the conclusions, so all legs regardless of the presence of holes were retained in the analysis in section 6. Where T_R encountered missing beams, the slope of the particle trajectory over three points before the particle encountered the missing data was calculated. Using the slope, the start altitude of the particle on the other side of the gap was calculated and the trajectory continued. Pairs of trajectories were calculated for 103 flight legs where the WMKA seeding aircraft intersected the UWKA flight track. Of these, 75 pairs landed within the domain. The horizontal distance traveled for these 75 pairs of trajectories was calculated and compared. The outcome of all trajectories is summarized in Table 1.

For the purposes of this research, the landing point of T_R and T_F was analyzed on the basis of where the IPC targets during their cloud seeding missions along the UWKA cross section. In the figures referenced in section 6, the IPC target regions are marked by the green terrain outline, and the end points of T_R and T_F were analyzed relative to those regions.

6. Results

In this section comparisons of particle trajectories are shown for individual flight legs that encompass the range of scenarios representing the overall behavior of the trajectories for all intersections between UWKA and WMKA during SNOWIE. The cases presented here are ordered based on the along track component of the 700-hPa wind speed from weakest to strongest; 700 hPa is just below the seeding level. In some cases, more than one example is shown at similar 700-hPa wind speeds since the trajectories evolved very differently. In section 7, a statistical summary of data for all trajectories is presented.

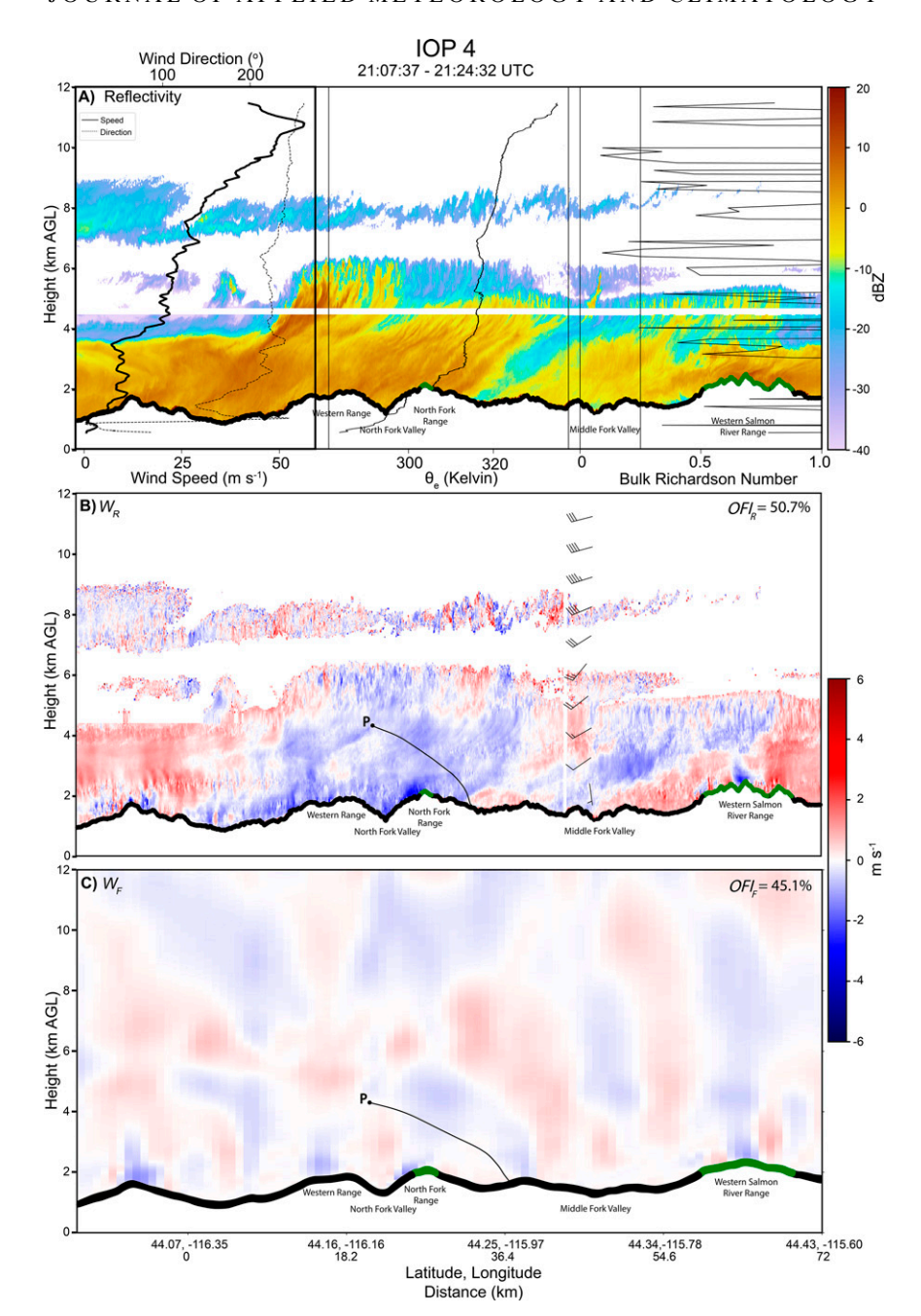


FIG. 8. Vertical cross sections from IOP4 2107:37–2124:32 UTC 18 Jan 2017. (a) Z_e , with wind speed (thick line), wind direction (thin line), θ_e , and R_b from the rawinsonde launched at 2200 UTC from Crouch overlayed, (b) vertical motion field and trajectory (black line where P is the location of the seeding aircraft) using w_R [wind speed (m s⁻¹) and direction (a flag is 50 m s⁻¹, a full barb is 10 m s⁻¹, and a half barb is 5 m s⁻¹) from WRF at the location over the Middle Fork valley at the nearest hour are also plotted], and (c) vertical motion field and trajectory (black line where P is the location of the seeding aircraft) using w_F . In all panels, terrain <2000 m and below the IPC target elevation is colored black. Terrain with elevations >2000 m and within IPC target elevation is colored green.

a. $IOP \ 4 \ FL \ 4 \ (9.7 \ m \ s^{-1}, \ OFI_R = 50.7\%, \ and \ OFI_F = 45.1\%)$

Figure 8a shows a stratiform cloud with generating cells at cloud top at ~6 km. Rawinsonde data from 2200 UTC

at Crouch shows wind speeds increased from the surface at 2 to 5 m s⁻¹ from 165° at 1.6 km and 10 m s⁻¹ from 240° at 3.7 km. The WRF wind component in the direction of the cross section at 700 hPa was ~10 m s⁻¹; θ_e increased with

height from the valley to \sim 5 km. Between 5 and 6 km, θ_e decreased with height over a shallow layer, consistent with presence of the cloud-top generating cells. $R_b > 0.25$ over a significant depth within the cloud, indicating that the environment was not supportive of shear-induced turbulence.

The particles in T_R during IOP 4 FL 4 (Fig. 8b) traveled 11.3 km downstream from P, one of the shortest distances traveled by particles in the observations of the 75 pairs of trajectories. At 4 km, the WRF horizontal wind was from the west southwest at ~15 m s⁻¹ and decreased in speed to <5 m s⁻¹ within the Middle Fork valley. There were minimal updrafts in w_R over the Western Range, North Fork valley, and North Fork Range. The combination of weak horizontal winds and downdrafts caused the slope of T_R to be relatively steep, limiting the distance traveled by the particle (Fig. 8b). T_F traveled ~4.4 km farther than T_R because the 900-m model did not resolve the strength or the widespread nature of the downdrafts influencing the trajectory. The model generated an updraft in the North Fork valley and had downdrafts \sim 2 m s⁻¹ weaker than w_R above the North Fork Range. These differences reduced the magnitude of the slope of T_F and caused the particle to reach the ground farther east than in T_R (Fig. 8c). Both T_R and T_F landed in the Middle Fork valley at a lower elevation than the target elevation.

b.
$$IOP\ 14\ FL\ 3\ (13.3\ m\ s^{-1},\ OFI_R = 52.8\%,\ and\ OFI_F = 54.7\%)$$

Figure 9 shows cross sections of reflectivity, w_R , and w_F from a stratiform cloud in IOP 14 with cloud-top echo reaching ~9 km. Rawinsonde data showed weak and variable winds below 2.1 km. From 2.1 to 4.0 km the wind speed increased from 5 to 16 m s⁻¹ and increased further from 16 to 40 m s⁻¹ between 4 and 8 km. The wind direction remained near 200° above 2 km to cloud top. In general, θ_e increased throughout the depth of the cloud indicating stable stratification. The shear was insufficient to generate turbulence based on the profile of R_b .

The difference between T_R and T_F was one of the smallest of the 75 pairs of trajectories calculated from SNOWIE. The w_R cross section showed weak circulations forced by the orography and weak, transient boundary layer turbulence, each with magnitudes of $\sim 1 \text{ m s}^{-1}$ (Fig. 9b). The 900-m-resolution model resolved the orographically forced vertical circulations; however, they were narrower than what was observed. In Fig. 9b, between 18.8 and 54.5 km, there were three wide, orographically forced updrafts that merged with increasing altitude. From 18.8 to 54.5 km in Fig. 9c there were approximately four updrafts forced by the terrain that remained narrow and distinct throughout the depth of the cross section. OFI_R and OFI_F were similar because the difference in updraft structure was minimal, and it did not significantly affect T_R and T_F because the particles traveled lower in the cloud where the updrafts were narrow in the observations and the model. Since the updrafts were weak, the strongest influence on particle motion was the along-flight component of the wind and the terminal velocity that was the same in T_R and T_{F} . The WRF horizontal winds were out of the southwest with

speeds of \sim 15 m s⁻¹ between 3 and 4 km before becoming southeasterly near the ground. The difference between T_R and T_F was \sim 806 m. Both particles fell in the narrow North Fork valley at an elevation lower than the ideal target elevation.

c. IOP 11 FL 5 (17.4 m s⁻¹,
$$OFI_R = 59.4\%$$
, and $OFI_F = 69.9\%$)

Figure 10a shows the reflectivity and rawinsonde data for a 6-km-deep stratiform orographic cloud from IOP 11. Between 3 and 5 km the wind speed was nearly constant between 14 and 16 m s⁻¹. The greatest change in wind speed occurred between the base of the valley and 2 km where wind speeds increased from \sim 0 to 14 m s⁻¹ and between 5 and 6 km where wind speeds increased from 16 to 30 m s⁻¹. Above 2 km, the wind direction was 240°–250° throughout the depth of the cloud; θ_e was almost constant with height from \sim 1.5 to 3.8 km before decreasing with height at 3.8 km. The w_R cross section (Fig. 10b) suggests that, in addition to orographically induced waves, boundary layer turbulence occurred near the mountain peak and possibly weak elevated convection on the east side of the cross section in the weakly unstable layer between 4 and 5 km.

Seeding material was released at the 4-km level. WRF horizontal winds were easterly at 15 m s⁻¹ below 3 km and increased to 20 m s⁻¹ between 3 and 4 km. When T_R (Fig. 10b) and T_F (Fig. 10c) were compared, the slopes of the particle trajectories were similar. As the particles fell, T_R and T_F both maintained near-continuous slopes as they passed through weak updrafts and downdrafts over the windward and leeward slopes of the Western Range and a stronger updraft over the windward slopes of the North Fork Range. In the Middle Fork valley, WRF had stronger updrafts and downdrafts causing T_F to have a steeper slope within the vertical circulations, resulting in the particle traveling a slightly shorter distance than T_R . The relatively weak horizontal winds at the level of the trajectories also limited their eastward extent. The distance that a particle traveled in T_R was 487 m farther than that traveled by the particle in T_F . The difference was small because the model captured the fixed, orographic waves that had the largest influence on particle trajectories. Despite the small difference in updraft structures, OFI_R and OFI_F differed by ~10% because of the boundary layer turbulence in the observations. The T_R and T_F both reached the ground in a valley upstream and at a lower elevation than the ideal IPC target.

d.
$$IOP \ 8 \ FL \ 4 \ (21.1 \ m \ s^{-1}, \ OFI_R = 49.9\%, \ and \ OFI_F = 60.9\%)$$

IOP 8 captured an ~7.5-km stable, deep cloud with strong wind shear below 4 km while above 4 km the winds were nearly constant with height. The data overlayed on Fig. 11a were from a rawinsonde launched at 1800 UTC, 4 h before the flight leg. This was the closest sounding in time to the flight leg; however, given the 4-h difference, the environment may have changed between the launch of the rawinsonde and the flight leg. The wind profiles show winds increasing from near 0 m s⁻¹ in the valley to 22 m s⁻¹ at 4 km, shifting from ~140° to 200°. Above 5 km to cloud top, wind speeds varied around ~22 m s⁻¹. The θ_e was

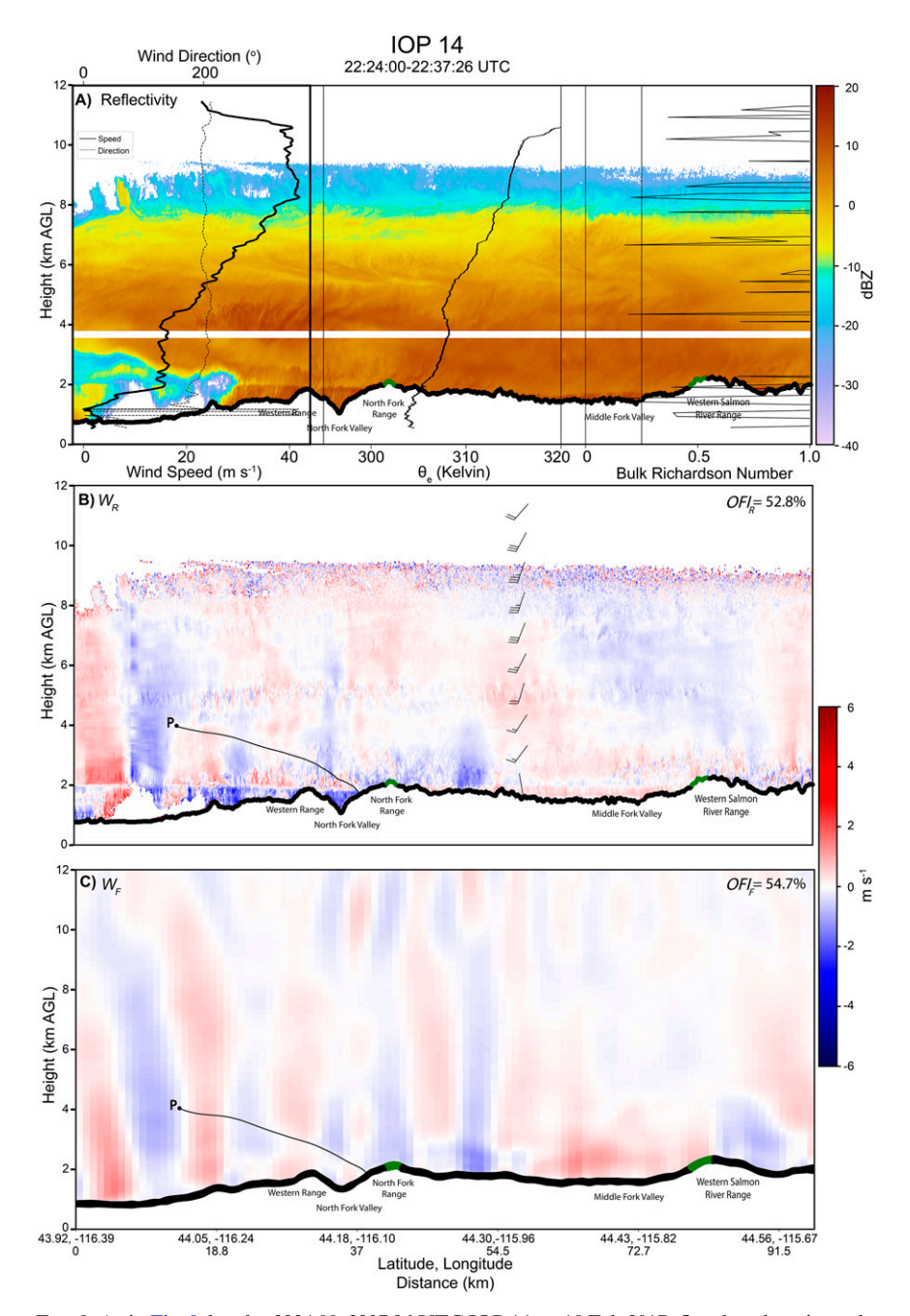


FIG. 9. As in Fig. 8, but for 2224:00–2237:26 UTC IOP 14 on 18 Feb 2017. Overlayed rawinsonde data were from Lowman at 2200 UTC.

almost constant with height from within the valley to cloud top indicating a weakly stable atmosphere. The R_b was <0.25 below 3 km where shear-generated turbulence was present.

IOP 8 FL 4 was one of eight pairs of trajectories for which both T_F and T_R did not land before reaching the east side of the cross section. Figure 11b shows broad, weak orographic forcing and weak-shear-induced turbulence below $\sim 3~\rm km$ within regions of weak, downdrafts. The cross section from the 900-m model (Fig. 11c) captured orographically forced

updrafts that were wider in the model than in the observations but similar in magnitude. The weak, broad updrafts and downdrafts, in an environment with $\sim\!\!20~{\rm m~s}^{-1}$ WRF winds between 2.5 and 4 km, supported particle trajectories that fell $\sim\!\!2$ km before exiting the east side of the cross section. This flight leg was $\sim\!\!55$ km in length, whereas other flight legs were $\sim\!\!72\!-\!92$ km in length. Since the trajectories did not land before exiting the cross section, it could not be determined if the particles landed at an ideal target altitude.

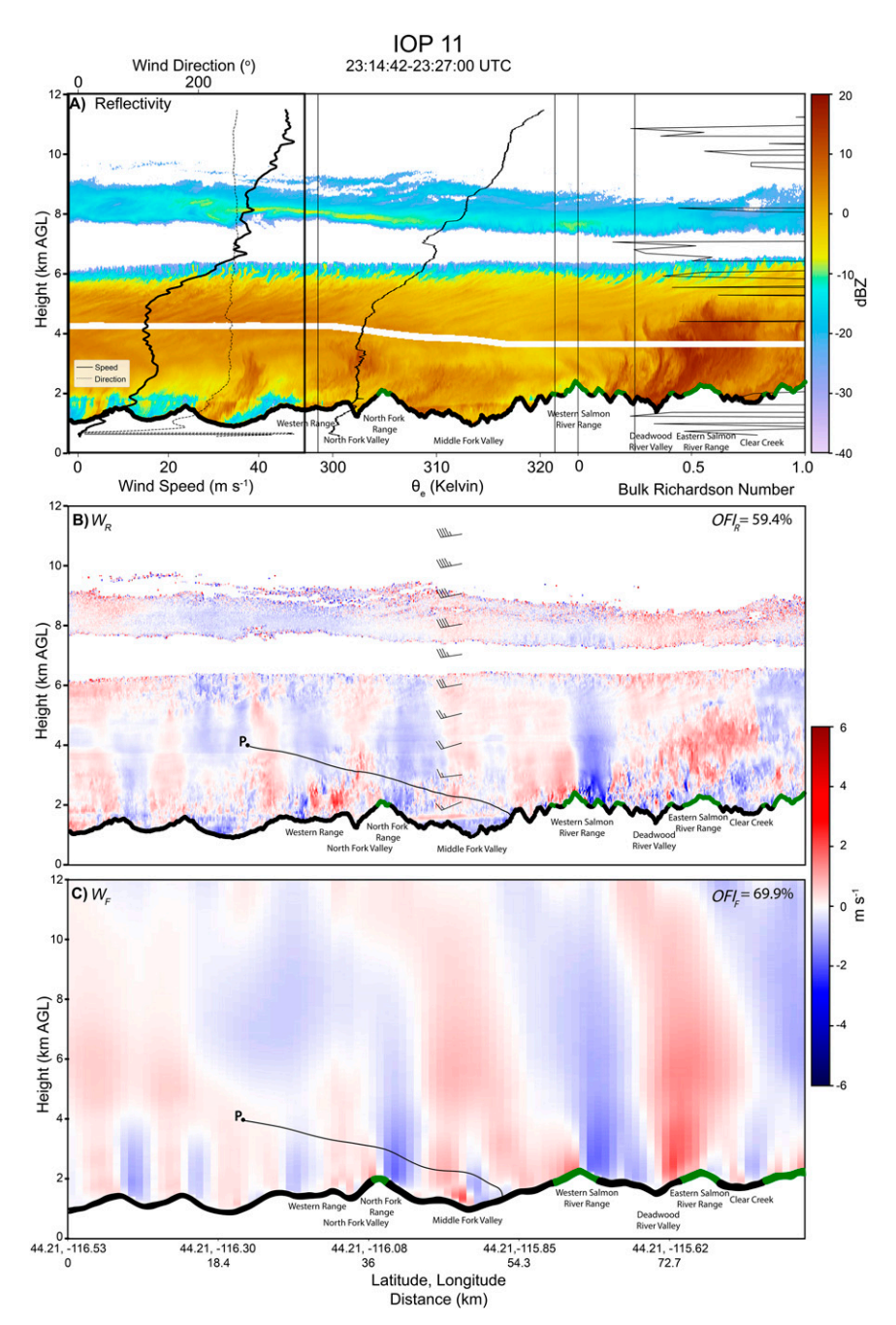


FIG. 10. As in Fig. 8, but for 2314:42–2327:00 UTC IOP 11 on 4 Feb 2017. Overlayed rawinsonde data were at 2300 UTC from Crouch.

e. $IOP\ 20\ FL\ 6\ (21.4\ m\ s^{-1},\ OFI_R = 49.4\%,\ and\ OFI_F = 73.2\%)$

IOP 20 FL 6 was similar to IOP 16 with strong, transient features above P that were not captured by the model. Figure 12b shows gravity waves between 4 and 6 km that initiated elevated convection above that level. The gravity waves were associated with maximum updrafts of \sim 6 m s⁻¹ and the elevated convection associated with updrafts of \sim 5 m s⁻¹.

Zaremba et al. (2022b) described this event and noted that the gravity wave features may have been initiated by an approaching cold front. Rawinsonde data from Crouch at 1300 UTC showed wind speeds increasing from 2 m s⁻¹ at 160° in the valley to 16 m s⁻¹ at 210° at 2.1 km. Between ~2.0 and 5.4 km wind speed varied between 15 and 25 m s⁻¹ before increasing to ~38 m s⁻¹ at cloud top. Within the gravity wave layer, the winds back with height from ~225° at ~3.8 km to ~195° at ~5.7 km; θ_e was constant with height from the

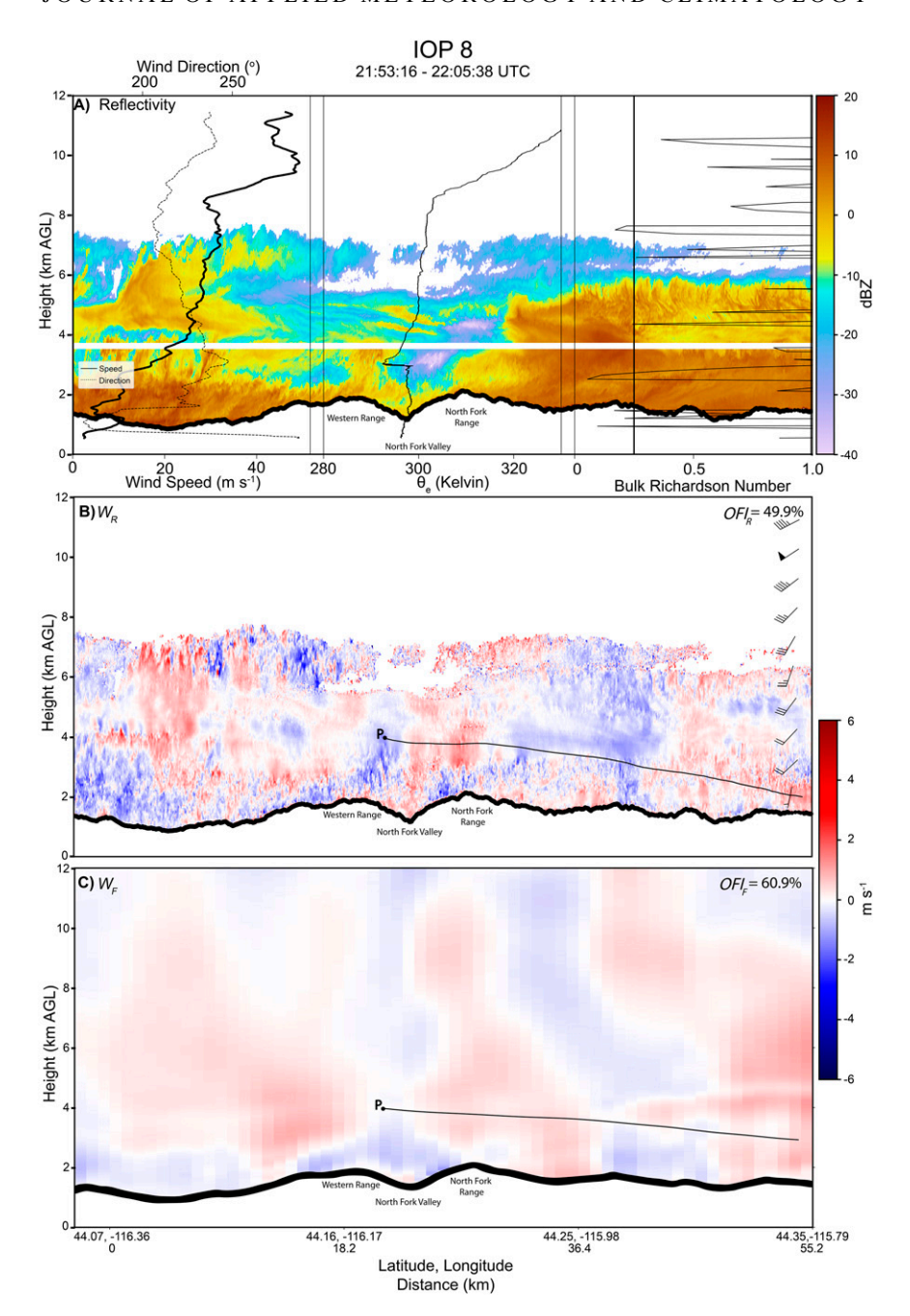


FIG. 11. As in Fig. 8, but for 2153:16–2205:38 UTC IOP 8 on 22 Jan 2017. Overlayed rawinsonde data were from 1800 UTC at Crouch.

valley to \sim 3 km and increased with height from 3.0 to 6.2 km, indicating a weakly stable environment. The R_b was less than 0.25 near cloud top and in two narrow layers below the base of the layer containing the gravity waves. The environment and updraft structures of this case are described in more detail in Zaremba et al. (2022b).

Downdrafts with a magnitude of 1–2 m s⁻¹ and weak updrafts associated with shear turbulence and orographic forcing along the windward side of the Western Salmon River Range

were the dominant vertical circulations below 4 km. In Fig. 12c, the model generated low-level orographic waves with maximum updrafts of \sim 3 m s⁻¹ between 2 and 4 km, 2 km below the gravity waves in the observations. The updrafts associated with these waves extended from the mountain crests to the top of the cross section, indicating that the waves were generated by the terrain. This was further supported by an OFI_F of 73.2%, which was \sim 24% greater than OFI_F. Above 4 km in Fig. 12c, the shorter wavelength waves

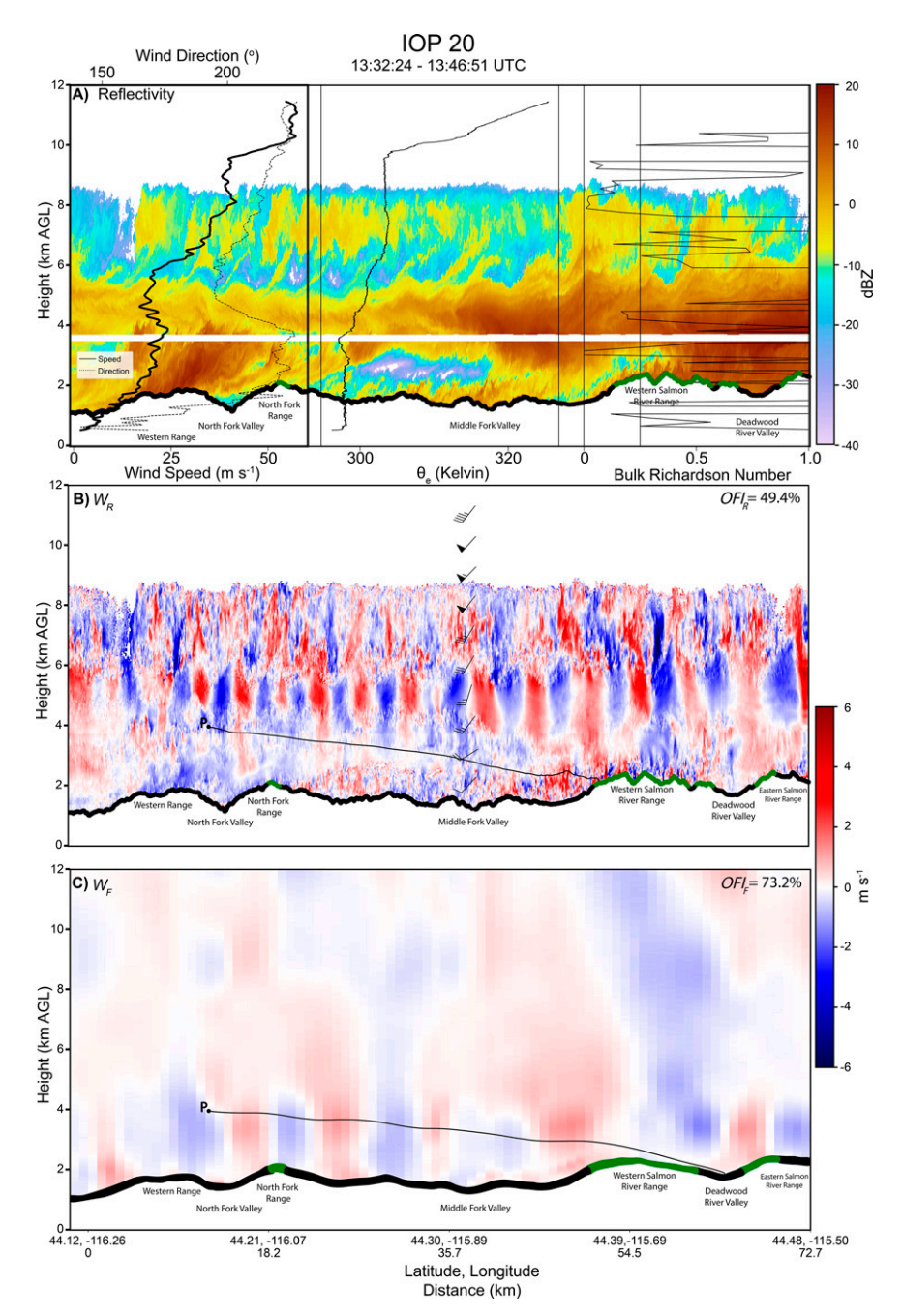


FIG. 12. As in Fig. 8, but for 1332:24–1346:51 UTC IOP 20 on 5 Mar 2017. Overlayed rawinsonde data were from 1300 UTC at Crouch.

took on a longer wavelength and did not initiate stronger updrafts above it. The orographically forced updrafts on the upwind slope of the Western and Eastern Salmon River Range were one of the few updraft features seen in both w_R and w_F . Seeding particles in T_R and T_F started at 4 km at an altitude at which the WRF horizontal winds were ~25 m s⁻¹ out of the southwest, decreasing to ~20 m s⁻¹ by 3 km. At 2 km, the WRF winds decreased to ~10 m s⁻¹; T_R reached the terrain slightly above 2000 m while T_F landed in the valley to the east and

slightly below 2000 m. The wind was relatively strong for the entire duration of T_R and T_F , which transported the particles farther east than the previous IOPs. Between 18.2 and 35.7 km, T_R had a steeper slope than T_F . In this region, the model generated an orographically forced wave between the surface and 3–4 km, whereas there were more turbulent features in the same region in the observations. As a result, the updrafts in w_F lofted the particles while the downdrafts in w_R caused the particles to fall. The inconsistency

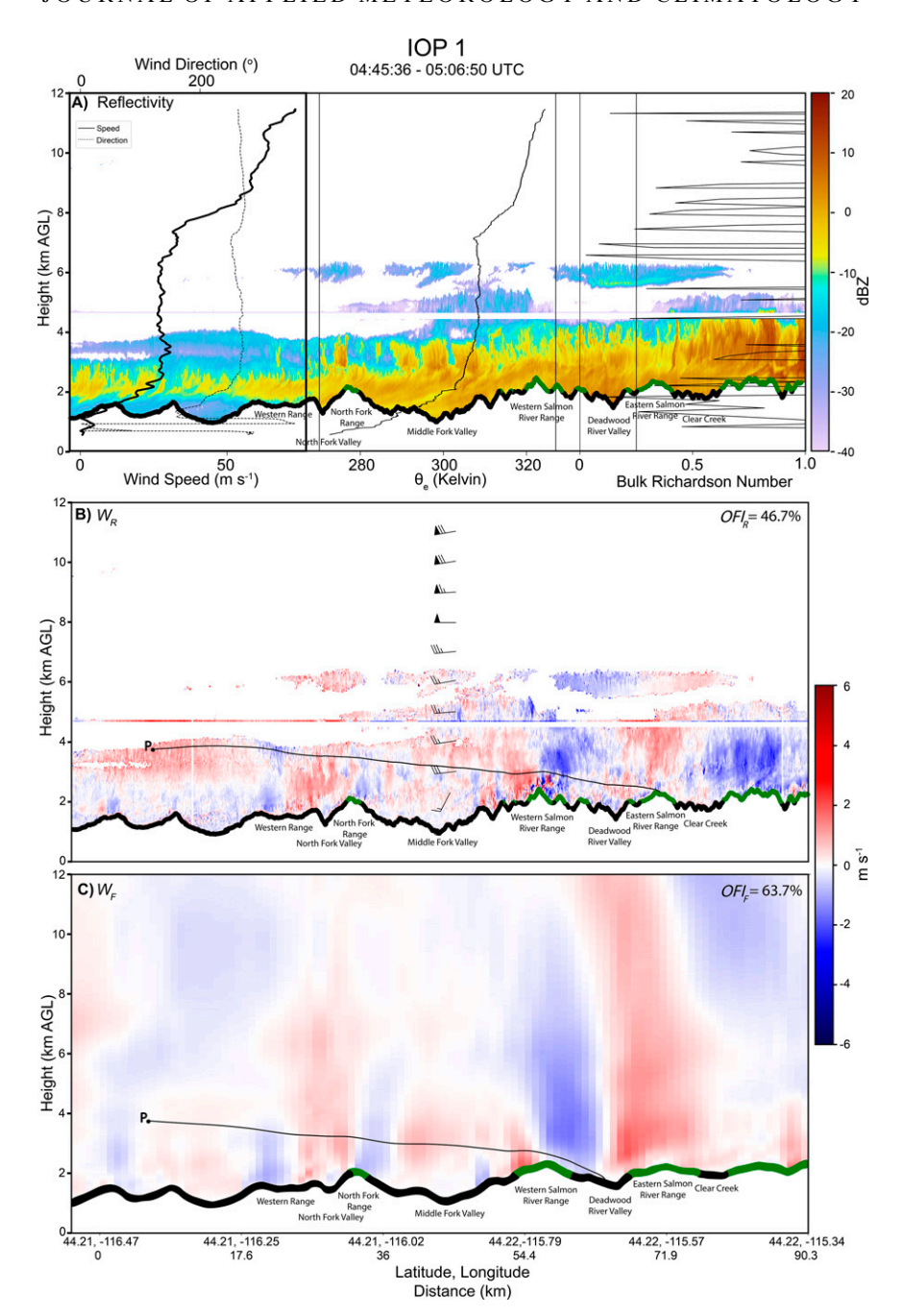


FIG. 13. As in Fig. 8, but for 0445:36–0506:50 UTC during IOP 1 on 8 Jan 2017. Overlayed rawinsonde data were from 0400 UTC at Crouch.

in updraft structures between 18.2 and 35.7 km in the model and the observations caused the particles in T_R to hit the windward side of the Western Salmon River Range rather than being carried over the peak by the orographically forced updraft in w_F . The difference between T_F and T_R was 12.9 km. As a result, the particles in the model landed within a valley whereas the particles in the observations landed at a higher elevation.

f. IOP 1 FL 8 (25.6 m s⁻¹, $OFI_R = 46.7\%$, and $OFI_F = 63.7\%$)

Figure 13a shows a 4-km-deep cloud on the western side of the cross section, with cloud tops reaching 5 km to the east. Rawinsonde data from 0400 UTC 8 January show wind speeds increasing sharply from near 0 m s⁻¹ in the valley to ~28 m s⁻¹ at 2.7 km. Above 2.7 km wind speed and direction remained almost constant between 25 and 30 m s⁻¹ at 250°–270°. The atmosphere

was stable below \sim 2.7 km where θ_e increased with height and became weakly stable above 2.7 km to cloud top, where θ_e was constant with height.

Figures 13b and 13c show the trajectories from IOP 1 FL 8 where the particles in w_R traveled ~64.7 km, the farthest distance traveled by particles in the observations where particles in the observations and WRF both landed in the domain. The horizontal winds between 3 and 4 km from WRF were westerly at \sim 25–30 m s⁻¹. The relatively strong winds decreased to calm within the valley. The cross section of w_R shows that there were multiple updrafts caused by shear turbulence and orographic forcing. These updrafts were strong enough to hold the particles at an altitude between 3 and 4 km where the WRF wind speeds were relatively strong. A 1-km layer of relatively strong winds and multiple updrafts supported a nearly horizontal trajectory for over 60 km before the particles landed on the Eastern Salmon River Range in the observations and in the Deadwood River valley in WRF. Figure 13c shows that the 900-m model resolved the updraft structures well except for the downdraft in the lee of the Western Salmon River Range and the updraft on the windward side of the Eastern Salmon River Range. The more widespread downdraft in the lee of the Western Salmon River Range brought the particle to an altitude where it could not be carried over the Eastern Salmon River Range. The difference in OFI_R and OFI_F is likely associated with boundary layer turbulence in the observations. These differences contributed to the particle in the observations landing above the ideal elevation while the particle in WRF landed in a lower-than-ideal elevation.

g.
$$IOP\ 17\ FL\ 4\ (28.1\ m\ s^{-1},\ OFI_R=51\%,\ and\ OFI_F=85.8\%)$$

In section 4b(2) the environment and cross sections of w_R and w_F from IOP 17 FL 4 (Fig. 14) were analyzed and showed fine-scale convective circulations embedded in fixed, orographic waves. The 900-m-resolution model resolved the orographic waves but failed to capture the fine-scale features associated with the convection, which is reflected in the difference between OFI_R and OFI_F. Figure 14 shows cross sections of w_R and w_F with trajectories of particles initiated by cloud seeding overlayed on the w profiles. T_R and T_F were initiated at \sim 4 km in a region of southwesterly winds at \sim 30 m s⁻¹ between 3 and 4 km; T_R had a more significant downward component than T_F because of the strong convective downdrafts. At 2 km the WRF winds become more southerly and weaken slightly to $\sim 25 \text{ m s}^{-1}$ as the particles approached the ground. Relatively strong winds near the terrain keep the negative slopes of T_R and T_F more horizontal than vertical despite the strong transient downdrafts. The model did not capture the structure of the convective downdrafts, which caused the particle in T_E to travel 7.6 km farther than the particle in T_R . On the upwind side of the first mountain in the Middle Fork valley, the model generated an updraft extending across the width of the windward slope of the mountain reaching the top of the cross section (Fig. 14c). Figure 14b shows that the updraft on the windward side of the mountain in the Middle

Fork valley in the observations was convective, and likely enhanced by the mountain, but did not result in a focused, orographically forced updraft. As a result, T_R fell faster within this region because there were small-scale downdrafts while particles following T_F were held higher in the cloud by an orographically forced updraft. The strength and prevalence of the small-scale downdrafts in w_R caused T_R to hit the ground sooner. Both trajectories landed in a valley at an elevation lower than the ideal target area. Since the valley was ~30 km wide, a 7.6-km difference between T_R and T_F was not enough to cause the particles to land in different parts of the target region.

h.
$$IOP\ 12\ FL\ 2\ (30.5\ m\ s^{-1},\ OFI_R=53.4\%,\ and\ OFI_F=68.1\%)$$

A shallow cloud with weak orographic forcing and elevated convection was present in IOP 12 FL 2. Cloud tops reached 4 km for a majority of the cross section except for convective towers that reached almost 6 km (Figs. 15a,b). Rawinsonde data from Crouch at 2000 UTC shows a potentially unstable layer between ~3.5 and ~4.5 km coinciding with the layer with convective towers. Within this layer the wind speed and direction were relatively constant at ~30 m s⁻¹ at ~265°. Below the elevated convection, the wind speed increased from near 0 m s⁻¹ within the valley to ~30 m s⁻¹ at ~3.5 km in a stable environment where θ_e increased with height.

The model generated a broad region of rising air on the east and west side of the cross section with a deep, orographically forced updraft and downdraft along the Western Salmon River Range (Fig. 15c). There were minimal similarities in updraft structures between Figs. 15b and 15c, which was reflected in the 14.2-km difference between distance traveled by particles in T_R and T_F , with OFI_R and OFI_F differing by ~15%. From 3 to 4 km the WRF horizontal wind was westerly at $\sim 30-35$ m s⁻¹. The seeding particles were released at ~3.5 km where the strong horizontal winds led to the slopes of T_R and T_F being near horizontal. The WRF wind speed decreased to ~ 5 m s⁻¹ at 1.5 km but T_R and T_F were at a higher altitude for a majority of their path. Above the Middle Fork valley, w_R contained widespread downdrafts strong enough to bring the particles to a lower altitude with weaker horizontal winds. In the same region, the model resolved weak updrafts strong enough to support the particles until encountering the downdraft in the lee of the Western Salmon River Range. As a result, T_R landed at an elevation just below the ideal target altitude on the windward side of the Western Salmon River Range while T_F landed at an elevation just below the ideal target altitude in the Deadwood River valley.

7. Discussion

In general, the 900-m WRF simulations accurately captured updraft structures that occur on scales large enough to be resolved by a 900-m model. The resolved updraft structures tend to be fixed, orographically forced waves as shown in Fig. 4. Zaremba et al. (2022b) compared the composites of w_R cross sections and w_F cross sections from SNOWIE and found

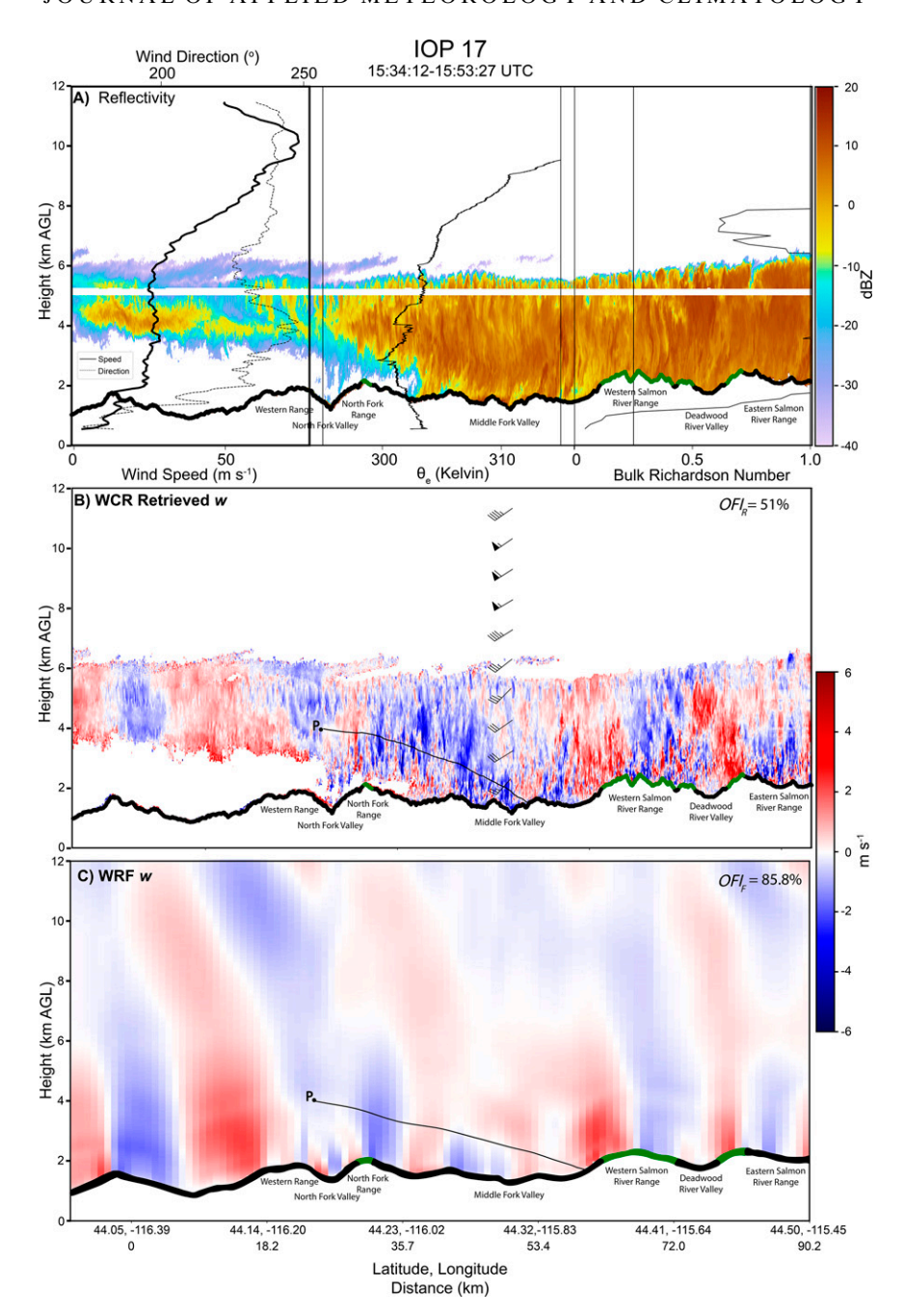


Fig. 14. As in Fig. 8, but for 1534:12–1553:27 UTC IOP 17 on 21 Feb 2017. Overlayed rawinsonde data were from 1600 UTC at Crouch.

that the composite cross sections, which largely filtered transient updrafts, matched the model simulated updrafts in both magnitude and location. Since coarser-resolution models (>900 m) are used for forecasting cloud seeding missions, it is important to understand how transient updrafts and downdrafts affect the trajectories of particles generated by cloud seeding. Cloud seeding over the Payette basin normally occurs at the level from -12° to -15° C, which is typically

between 3 and 4 km MSL, so only the vertical motion structures below 4 km impact particle trajectories.

The scatterplot in Fig. 16a summarizes the 75 pairs of trajectories that were compared from SNOWIE. In this figure, flight legs are categorized by OFI_R and the landing elevation of the trajectories. High terrain was defined as >2000 m, which is the ideal minimum target elevation for cloud seeding used by IPC because the main goal of their cloud seeding

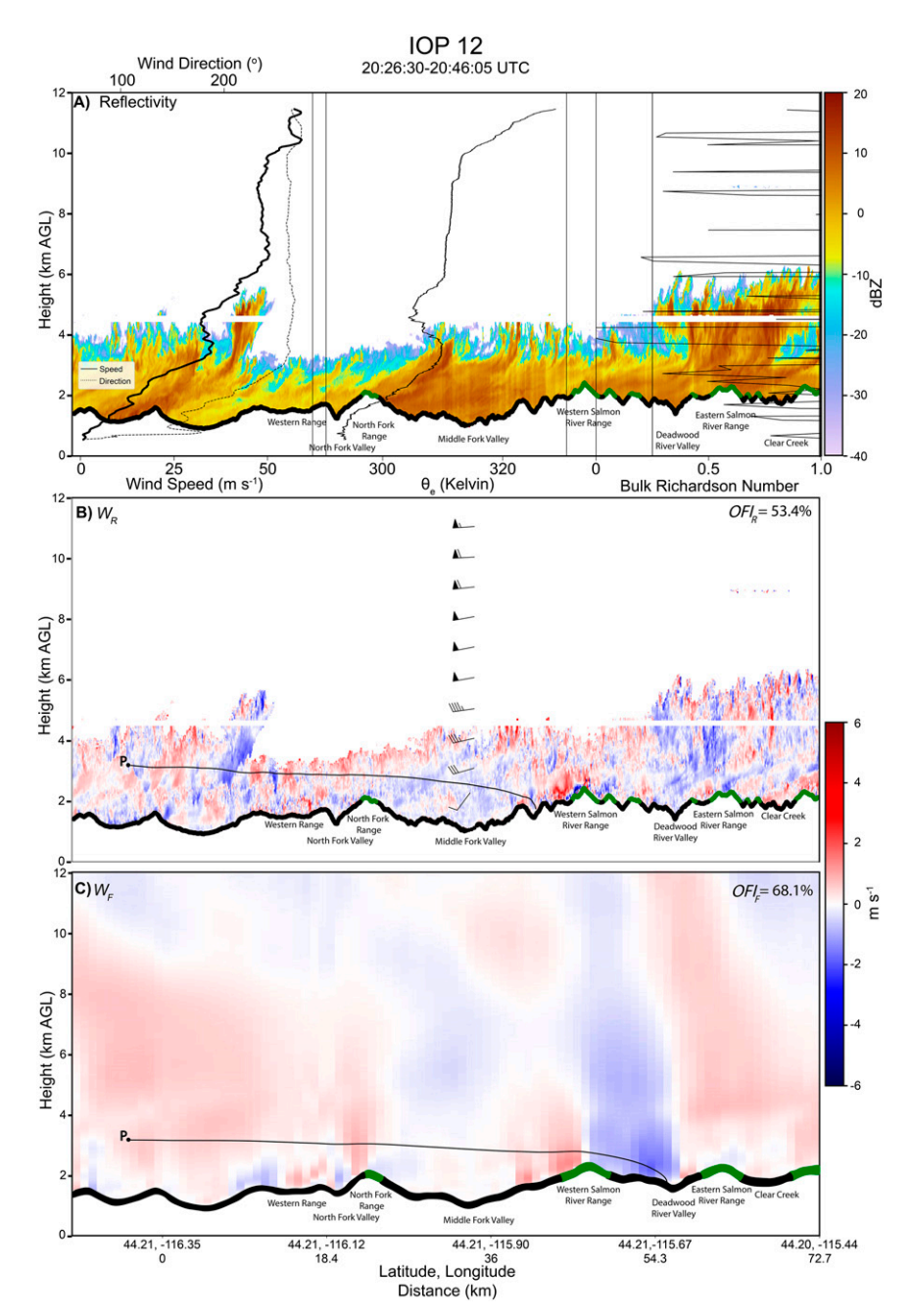


Fig. 15. As in Fig. 8, but for 2026:30–2046:05 UTC IOP 12 on 7 Feb 2017. Overlayed rawinsonde data were from 2000 UTC at Crouch.

effort is to build snowpack and extend the runoff season. Low terrain was defined as <2000 m.

It is seen that 66.7% of the flight-leg pairs are located between the one-to-one line and the 5-km lines, 21.3% fall between the 5- and 10-km lines, and 12% are associated with differences greater than 10 km. Small and large dots are found between each line, indicating transient features have a minimal effect on the distance traveled by particles. A similar story is shown in Fig. 16b where flight legs with small OFI_R

percentages are associated with minimal differences between T_R and T_F and flight legs with greater OFI_R percentages occur in cases with large differences between T_R and T_F . Overall, the average difference in distance traveled between T_R and T_F was ~ 5.1 km, with T_F traveling farther than T_R 74.7% of the time. The correlation coefficient of T_R and T_F was 0.92.

The black and green dots in Fig. 16a represent trajectories for which both the model and observations either land above the ideal target elevation (green) or below the ideal target

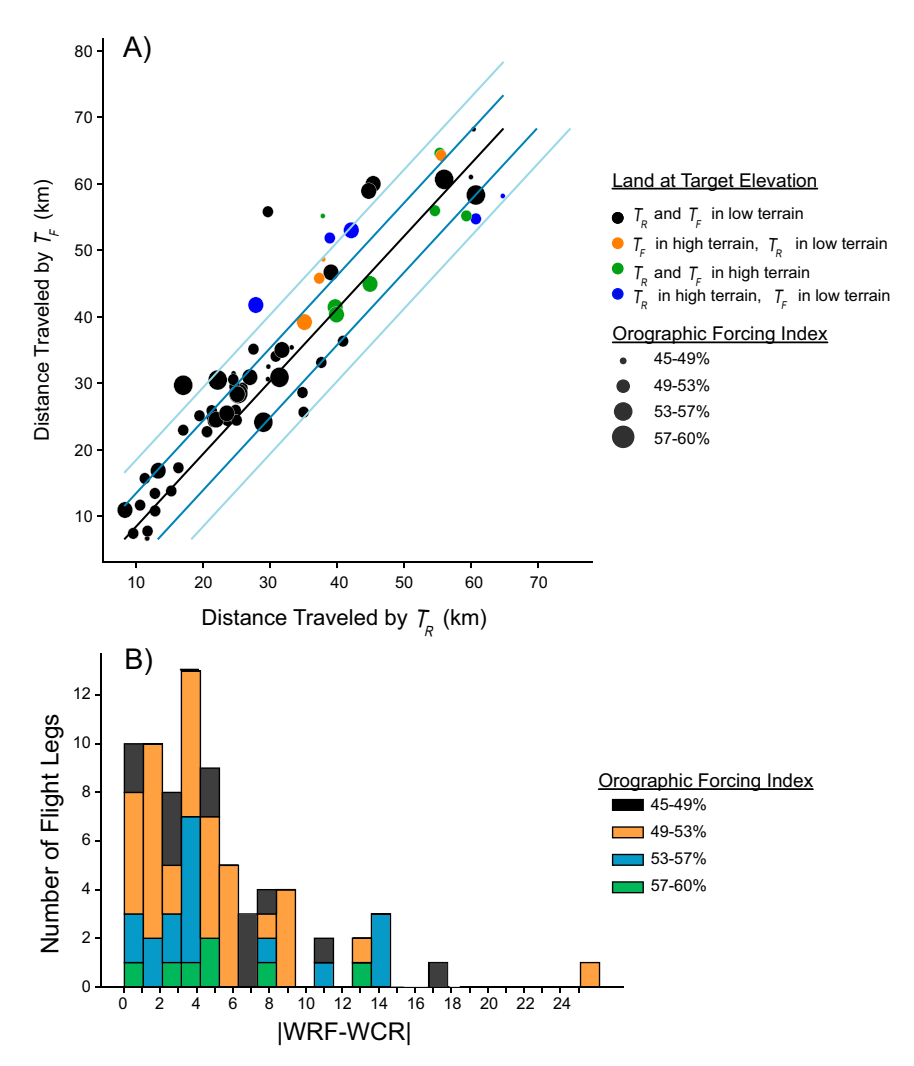


FIG. 16. (a) A scatterplot of the distance traveled by T_R vs the distance traveled by T_F , where each dot represents one of the 75 flight legs for which trajectories could be calculated. The black line marks the one-to-one line, the dark blue lines mark a 5-km difference between T_R and T_F , and the light-blue lines mark a 10-km difference between T_R and T_F . The flight legs were categorized by ${\rm OFI}_R$ and the elevation where they landed. Larger dots represent flight legs with a greater ${\rm OFI}_R$, indicating more fixed, orographic updrafts and downdrafts. Smaller dots represent flight legs with a smaller ${\rm OFI}_R$, indicating more transient vertical circulations. Black dots mark flight legs for which both trajectories landed in terrain <2000 m, green dots mark flight legs for which both trajectories land at >2000 m, orange dots mark flight legs for which T_F lands at >2000 m and T_R lands at <2000 m, and blue dots mark flight legs for which T_R lands at >2000 m and T_R lands at <2000 m. (b) A stacked bar graph of the absolute difference of T_F - T_R for each flight leg. The colors correspond to ${\rm OFI}_R$ values.

elevation (black). Table 2 shows that in 58 (77.3%) pairs of cross sections T_R and T_F both landed at elevations lower than the ideal target elevation. This outcome is concentrated in cases in which particles travel less than 37 km. In many cross

sections (e.g., Figs. 10 and 14), particles are lifted above the upwind side of the mountain by orographically forced updrafts and then forced into a downstream valley within the basin by orographically forced downdrafts. Within the valley,

TABLE 2. Outcomes for 75 pairs where T_R and T_F land relative to the ideal target area in each flight leg.

T_R and T_F land above the ideal target elev (>2000 m)	T_R and T_F do not land above the ideal target elev	Only T_R lands above the ideal target elev	Only T_F lands above the ideal target elev
7	58	5	5

there were often weak winds causing the particles to become trapped in the valley and fall to an elevation <2000 m. The green dots, where both trajectories land in higher terrain, all occur where particles travel more than 37 km because they travel past the Middle Fork valley and land in the higher terrain of the Payette River basin. All of the 10 (13.3%) cases in which T_R and T_F differ in their landing elevation (orange and blue dots, see Table 2) had an OFI $_R$ value of less than 54%. This shows that, even though it is not common, the 900-m-resolution model is more likely to forecast a different landing elevation than the observations in more transient cases.

8. Conclusions

This paper examined the impact of fixed versus transient updrafts in orographic environments on the trajectories of ice particles created by airborne seeding by comparing particle trajectories through vertical motion fields retrieved from analysis of WCR data with vertical motion fields simulated by WRF at 900-m horizontal resolution. The WCR measurements were obtained as part of the SNOWIE field campaign. Through calculations of the orographic forcing index, the WRF simulation was shown to more often capture the fixed circulations forced by the orography but not subgrid-scale transient circulations associated with instability and shear. Trajectories of particles were calculated with identical horizontal wind and terminal velocity fields, but different updraft structures based on the observations and model simulation.

Particle trajectories were calculated for 103 pairs of cross sections, with each pair differing only by the vertical motion field. One member of the pair used derived vertical motions from WCR while the other member of the pair used vertical motions from the 900-m WRF simulation at the closest hour. Horizontal wind fields and particle terminal velocities were identical in both members of the pair so that the impact of the transient vertical circulations on particle trajectories could be isolated. The impacts of transient vertical motion features on particle trajectories were as follows:

- The distance traveled by particles upon reaching the ground in the model differed by <5 km from the particles in the observations in 66.7% of pairs of flight legs. The difference between the distance particles traveled in the observations and model was not heavily influenced by transient versus fixed, orographic features. The largest difference of distance traveled by particles occurred in conditions where convection was present.
- In 77.3% of the cases, the model and the observations agreed that particles landed at <2000 m in elevation. In 9.3% of cases, the model and observations agreed that the particles landed at >2000 m. In 13.3% of cases, the model and observations differed in where the particle landed with respect to the ideal target landing elevation of 2000 m.
- In 94.2% of cases in which particles traveled less than 37 km in the observations, particles in the observations and model descended into valleys. All cases in which the model and observations agreed that particles landed at elevations

- >2000 m occurred when the particles traveled more than 37 km. Particles traveled more than 37 km in both transient and fixed, orographic updraft-dominant cases when strong winds were present.
- In many pairs of trajectories, particles were lifted above the upwind side of the mountain by orographically forced updrafts and then forced into the downstream valley by orographically forced downdrafts on the lee side of the ridges.

The findings from this study show that, during airborne seeding operations, transient updrafts and downdrafts minimally impact the distance particles travel and the landing elevation of particles with respect to the ideal target elevation. The horizontal wind speeds between 3 and 4 km and updrafts over the Middle Fork valley have a larger influence on particle trajectory distance and landing elevation because these winds and updrafts determine whether particles travel to the higher terrain on the east side of the Middle Fork valley. For this reason, the updraft structures in the 900-m model appears to be sufficient to forecast the landing elevation of particles with respect to the 2000-m elevation level and the distance traveled by particles.

Acknowledgments. We thank the crews from the University of Wyoming King Air and the Weather Modification, Inc., King Air, as well as all students from the Universities of Colorado, Wyoming, and Illinois for their help in operating and deploying instruments during the campaign. Funding for the UWKA was provided through the National Science Foundation (NSF) Awards AGS-1361237 and AGS-1441831. Funding for seeding aircraft was provided by Idaho Power Company. The research was supported under NSF Grants AGS-1547101, AGS-1546963, AGS-1546939, AGS-2016106, AGS-2015829, and AGS-2016077. This material is based upon work supported by the National Center for Atmospheric Research (NCAR), which is a major facility sponsored by NSF under Cooperative Agreement 1852977. The first author was hosted, virtually because of COVID-19, at the Research Applications Laboratory at NCAR in the summer of 2020 as a visiting undergraduate researcher.

Data availability statement. All data presented here are publicly available through the SNOWIE data archive website (https://data.eol.ucar.edu/master_lists/generated/snowie/) maintained by the Earth Observing Laboratory at NCAR. Specific datasets can be accessed as follows: University of Wyoming King Air data: https://doi.org/10.15786/M2MW9F; University of Wyoming Cloud Radar data: doi:10.15786/M2CD4J; Idaho Power Crouch sounding data: https://doi.org/10.5065/D6J38R93; Idaho Power Lowman sounding data: https://doi.org/10.5065/D6NV9H02. The model simulation is archived with the NCAR Research Application Laboratory.

REFERENCES

Blestrud, D., 2018: Idaho Power Company Lowman Sounding Data. Version 1.2. UCAR/NCAR—Earth Observing Laboratory, accessed 5 September 2022, https://doi.org/10.5065/D6NV9H02.

- —, 2021: Idaho Power Company Crouch Sounding Data. Version 1.2. UCAR/NCAR—Earth Observing Laboratory, accessed 5 September 2022, https://doi.org/10.5065/D6J38R93.
- Bolton, D., 1980: Computation of equivalent potential temperature. *Mon. Wea. Rev.*, **108**, 1046–1053, https://doi.org/10.1175/1520-0493(1980)108<1046:TCOEPT>2.0.CO;2.
- Chu, X., L. Xue, B. Geerts, R. Rasmussen, and D. Breed, 2014: A case study of radar observations and WRF LES simulations of the impact of ground-based glaciogenic seeding on orographic clouds and precipitation. Part I: Observations and model validations. *J. Appl. Meteor. Climatol.*, 53, 2264–2286, https://doi.org/10.1175/JAMC-D-14-0017.1.
- —, B. Geerts, L. Xue, and B. Pokharel, 2017a: A case study of cloud radar observations and large-eddy simulations of a shallow stratiform orographic cloud, and the impact of glaciogenic seeding. J. Appl. Meteor. Climatol., 56, 1285–1304, https:// doi.org/10.1175/JAMC-D-16-0364.1.
- —, —, and R. Rasmussen, 2017b: Large-eddy simulations of the impact of ground-based glaciogenic seeding on shallow orographic convection: A case study. *J. Appl. Meteor. Climatol.*, **56**, 69–84, https://doi.org/10.1175/JAMC-D-16-0191.1.
- Garvert, M. F., B. Smull, and C. Mass, 2007: Multiscale mountain waves influencing a major orographic precipitation event. J. Atmos. Sci., 64, 711–737, https://doi.org/10.1175/JAS3876.1.
- Geerts, B., Q. Miao, and Y. Yang, 2011: Boundary layer turbulence and orographic precipitation growth in cold clouds: Evidence from profiling airborne radar data. *J. Atmos. Sci.*, 68, 2344–2365, https://doi.org/10.1175/JAS-D-10-05009.1.
- —, Y. Yang, R. Rasmussen, S. Haimov, and B. Pokharel, 2015: Snow growth and transport patterns in orographic storms as estimated from airborne vertical-plane dual-Doppler radar data. *Mon. Wea. Rev.*, **143**, 644–665, https://doi.org/10.1175/ MWR-D-14-00199.1.
- Grasmick, C., B. Geerts, J. R. French, S. Haimov, and R. M. Rauber, 2022: Estimating microphysics properties in ice-dominated clouds from airborne Ka-W band dual wavelength ratio reflectivity factor in close proximity to in situ probes. J. Atmos. Oceanic Technol., 39, https://doi.org/10.1175/JTECH-D-21-0147.1, in press.
- Hobbs, P. V., 1975a: The nature of winter clouds and precipitation in the Cascade Mountains and their modification by artificial seeding. Part I: Natural conditions. *J. Appl. Meteor. Climatol.*, 14, 783–804, https://doi.org/10.1175/1520-0450(1975)014<0783: TNOWCA>2.0.CO;2.
- —, 1975b: The nature of winter clouds and precipitation in the Cascade Mountains and their modification by artificial seeding. Part III: Case studies of the effects of seeding. *J. Appl. Meteor. Climatol.*, 14, 819–858, https://doi.org/10.1175/1520-0450(1975)014<0819:TNOWCA>2.0.CO:2.
- Holroyd, E. W., J. T. McPartland, and A. B. Super, 1988: Observations of silver iodide plumes over the grand mesa of Colorado. *J. Appl. Meteor. Climatol.*, **27**, 1125–1144, https://doi.org/10.1175/1520-0450(1988)027<1125:OOSIPO>2. 0,CO:2.
- Iacono, M. J., J. S. Delamere, E. J. Mlawer, M. W. Shephard, S. A. Clough, and W. D. Collins, 2008: Radiative forcing by long-lived greenhouse gases: Calculations with the AER radiative transfer models. *J. Geophys. Res.*, 113, D13103, https:// doi.org/10.1029/2008JD009944.
- Mielke, P. W., L. O. Grant, and C. F. Chappell, 1970: Elevation and spatial variation effects of wintertime orographic cloud

- seeding. J. Appl. Meteor. Climatol., 9, 476–488, https://doi.org/ 10.1175/1520-0450(1970)009<0476:EASVEO>2.0.CO;2.
- Nakanishi, M., and H. Niino, 2006: An improved Mellor–Yamada level-3 model: Its numerical stability and application to a regional prediction of advection fog. *Bound.-Layer Meteor.*, 119, 397–407, https://doi.org/10.1007/s10546-005-9030-8.
- Niu, G.-Y., and Coauthors, 2011: The community Noah land surface model with multiparameterization options (Noah-MP): 1. Model description and evaluation with local-scale measurements. *J. Geophys. Res.*, 116, D12109, https://doi.org/10.1029/2010JD015139.
- Rauber, R. M., R. D. Elliott, J. O. Rhea, A. W. Huggins, and D. W. Reynolds, 1988: A diagnostic technique for targeting during airborne seeding experiments in wintertime storms over the Sierra Nevada. *J. Appl. Meteor. Climatol.*, 27, 811–828, https://doi.org/10.1175/1520-0450(1988)027<0811:ADTFTD>2. 0.CO:2.
- —, and Coauthors, 2019: Wintertime orographic cloud seeding— A review. J. Appl. Meteor. Climatol., 58, 2117–2140, https://doi.org/10.1175/JAMC-D-18-0341.1.
- Research Flight Center, 2017a: Flight level data from the university of Wyoming king air during the Seeded and Natural Orographic Wintertime clouds—The Idaho Experiment (SNOWIE) project, version 1.0. University of Wyoming, College of Engineering, Department of Atmospheric Science, accessed 15 July 2022, https://doi.org/10.15786/M2MW9F.
- ——, 2017b: Wyoming cloud radar data from the university of Wyoming king air during the university of Wyoming king air during the Seeded and Natural Orographic Wintertime clouds—The Idaho Experiment (SNOWIE) project, version 1.0. University of Wyoming, College of Engineering, Department of Atmospheric Science, accessed 15 July 2022, https://doi.org/10.15786/M2CD4J.
- Tessendorf, S. A., and Coauthors, 2019: A transformational approach o winter orographic weather modification research: The SNOWIE project. *Bull. Amer. Meteor. Soc.*, **100**, 71–92, https://doi.org/10.1175/BAMS-D-17-0152.1.
- Thompson, G., and T. Eidhammer, 2014: A study of aerosol impacts on clouds and precipitation development in a large winter cyclone. *J. Atmos. Sci.*, **71**, 3636–3658, https://doi.org/10.1175/JAS-D-13-0305.1.
- Wendisch, M., and J.-L. Brenquier, 2013: Airborne Measurements for Environmental Research: Methods and Instruments, Wiley-VCH Verlag GmbH & Co. KGaA, 655 pp., https://doi.org/10. 1002/9783527653218.
- Xue, L., and Coauthors, 2013a: Implementation of a silver iodide cloud seeding parameterization in WRF. Part I: Model description and idealized 2D sensitivity tests. J. Appl. Meteor. Climatol., 52, 1433–1457, https://doi.org/10.1175/JAMC-D-12-0148.1.
- —, S. A. Tessendorf, E. Nelson, R. Rasmussen, D. Breed, S. Parkinson, P. Holbrook, and D. Blestrud, 2013b: Implementation of a silver iodide cloud seeding parameterization in WRF. Part II: 3D simulations of actual seeding events and sensitivity tests. *J. Appl. Meteor. Climatol.*, 52, 1458–1476, https://doi.org/10.1175/JAMC-D-12-0149.1.
- —, X. Chu, R. Rasmussen, D. Breed, B. Boe, and B. Geerts, 2014: The dispersion of silver iodide particles from ground-based generators over complex terrain. Part II: WRF large-eddy simulations versus observations. *J. Appl. Meteor. Climatol.*, 53, 1342–1361, https://doi.org/10.1175/JAMC-D-13-0241.1.

- —, —, —, and B. Geerts, 2016: A case study of radar observations and WRF LES simulations of the impact of ground-based glaciogenic seeding on orographic clouds and precipitation. Part II: AgI dispersion and seeding signals simulated by WRF. J. Appl. Meteor. Climatol., 55, 445–464, https://doi.org/10.1175/JAMC-D-15-0115.1.
- —, and Coauthors, 2017: WRF large-eddy simulations of chemical tracer deposition and seeding effect over complex terrain from ground- and aircraft-based AgI generators. *Atmos. Res.*, **190**, 89–103, https://doi.org/10.1016/j.atmosres. 2017.02.013.
- Zaremba, T. J., and Coauthors, 2022a: Vertical motions in orographic cloud systems over the Payette River basin. Part I: Recovery of vertical motions and their uncertainty from airborne Doppler radial velocity measurements. J. Appl. Meteor. Climatol., 61, 1707–1725, https://doi.org/10.1175/JAMC-D-21-0228.1.
- —, and Coauthors, 2022b: Vertical motions in orographic cloud systems over the Payette River basin. Part II: Fixed and transient updrafts and their relationship to forcing. *J. Appl. Meteor. Climatol.*, **61**, 1727–1745, https://doi.org/10.1175/JAMC-D-21-0229.1.